Title: Intermolecular Vibrational Energy Transfer Enabled by Microcavity Strong Light-Matter Coupling

Bo Xiang[1], Raphael F. Ribeiro[2], Matthew Du[2], Liying Chen[2], Zimo Yang[1], Jiaxi Wang[2], Joel Yuen-Zhou[2,*], Wei Xiong[1,2,*]

Affiliations:

[1] Materials Science and Engineering Program, University of California, San Diego, La Jolla, CA,92093

[2] Department of Chemistry and Biochemistry, University of California, San Diego, La Jolla, CA, 92093

*Correspondence to: joelyuen@ucsd.edu (Joel Yuen-Zhou) and w2xiong@ucsd.edu (Wei Xiong)

Abstract: Selective vibrational energy transfer between molecules in liquid phase, a difficult process due to weak intermolecular forces, is achieved through polaritons formed by strong coupling between cavity photon modes and donor and acceptor molecules. Using pump-probe and two-dimensional infrared (2D IR) spectroscopy, it is found that the excitation of the upper polariton, which is composed mostly of donors, can efficiently relax into the acceptors within 5 ps. The energy transfer efficiency can be further enhanced by increasing the cavity lifetime, suggesting the energy transfer is a polaritonic process. This remarkable vibrational energy transfer pathway opens doors for remote chemistry, sensing mechanisms, and vibrational polariton condensation.

Teaser: Light-matter strong coupling enables selective liquid-phase intermolecular energy transfer which is virtually absent in nature.

Vibrational energy transfer (VET) is ubiquitous to many molecular processes in the condensed phase, ranging from chemical catalysis (*1*, *2*) to biological signal transduction and molecular recognition (*3*, *4*). Due to through-bond anharmonic couplings, intramolecular and solute-solvent VET is widespread, leading to rapid intramolecular vibrational redistribution (IVR) that competes with other chemical events (*5*, *6*). However, through-space, selective intermolecular (solute-solute) VET is relatively rare. The scarcity of intermolecular VET is a consequence of weak intermolecular forces. Compared to electronic transitions, which readily undergo intermolecular energy transfer (via e.g., the Förster and Dexter mechanisms (*7*, *8*)), vibrational transition dipole moments are ten or hundred times smaller (*9*), leading to uncompetitive intermolecular dipole-dipole couplings when compared to their electronic counterparts (Fig.1a, top). As such, intermolecular VET is usually obfuscated by IVR.

Here, we report a state-of-the-art strategy to engineer intermolecular vibrational interactions via strong light-matter coupling. When a highly concentrated molecular sample is inserted into an optical microcavity (e.g., a Fabry-Perot (FP) cavity) or placed onto a plasmonic nanostructure (*10*), the confined electromagnetic modes interact reversibly with the collective macroscopic molecular vibrational polarization such that hybridized light-matter states, known as vibrational polaritons, are formed (*9–16*). Due to the delocalized nature of polaritons, the relaxation kinetics of strongly-coupled systems is substantially changed from their weakly-coupled counterparts (*13*). While pioneering studies have demonstrated such effects in the context of electronic energy transfer (*17–*

21), intermolecular VET under strong light-matter coupling seems to operate by different mechanisms, as we describe below. Furthermore, given the scarcity of selective intermolecular VET in condensed phases, its polaritonic counterpart introduces a powerful concept to alter the course of ground state chemistry in solution (*22*).

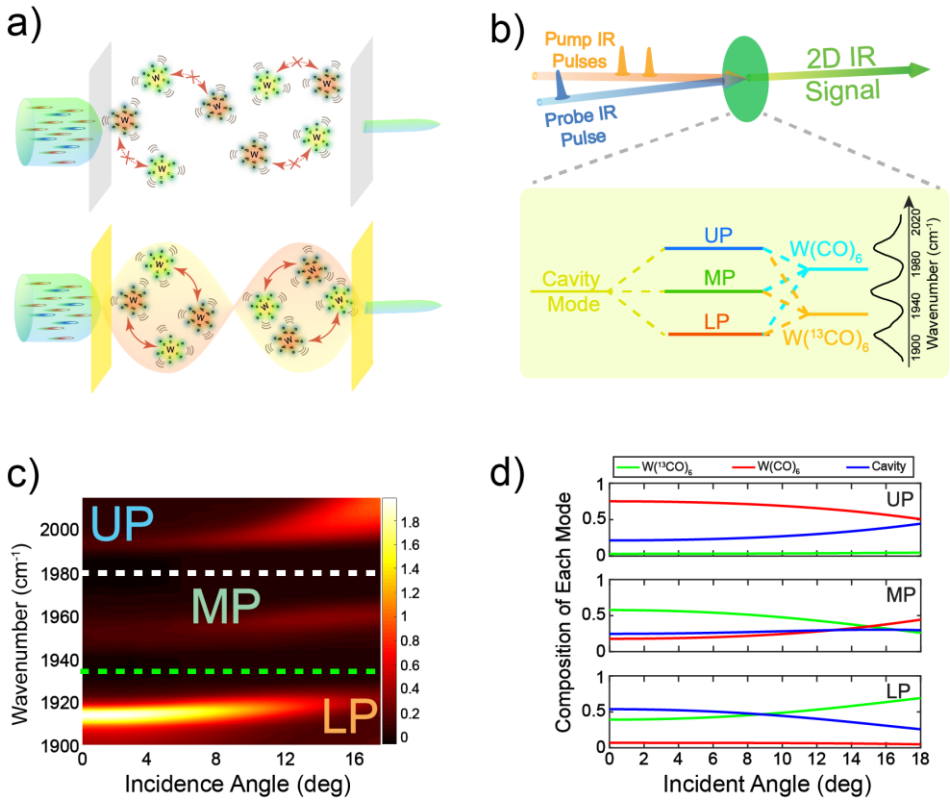

Fig. 1. Strongly coupled system between $W(CO)_6$, $W(^{13}CO)_6$ in a hexane-DCM mixture and a cavity. (a) Schematic illustration showing that VET between vibrational modes of $W(CO)_6$ and $W(^{13}CO)_6$ molecules is unfavorable in solution (top), while it is enabled by strong coupling of the molecular system to an infrared cavity mode (bottom). (b) Diagram of the 2D IR pulse sequence along with the IR spectrum and energy diagram of the system. (c) Transmission spectrum of the polaritonic system as a function of incidence angle; white and green dashed lines denote bare $W(CO)_6$ and $W(^{13}CO)_6$ vibrational transitions. (d) Hopfield coefficients for LP, MP, and UP as a function of incidence angle calculated as described in Supplementary Materials (SM) Section 11.

To study cavity-assisted intermolecular VET, we designed a strongly-coupled system composed of a microcavity and ensembles of two vibrational modes from different molecules. We encapsulated an equimolar solution of $W(CO)_6$ and $W(^{13}CO)_6$ in hexane/DCM solvent (total

concentration 100 mM, 1:1 volumetric ratio; see details in SM Materials and Methods) in a FP cavity. These molecules are ideal for achieving vibrational strong coupling, as they have degenerate asymmetric stretch modes with large oscillator strength and narrow linewidths. The cavity with thickness L has resonances at $\lambda = \frac{2}{n}L$, where n= *1,2,3, ...* is the cavity mode order. Because the carbonyl asymmetric stretches of $W(CO)_6$ and $W(^{13}CO)_6$ absorb at 1980 and 1938 cm^{-1}, respectively, a cavity with $L = n\times 2.5$ μm has modes which are nearly resonant with both vibrational transitions. In our experiments, unless specifically noted, we kept L at 12.5 μm and strongly coupled the 5th order cavity modes to the vibrations.

For each molecular subsystem, the light-matter coupling g is proportional to $\sqrt{C}$, where C is the concentration of the absorbers. Given a large enough C, each molecular subsystem satisfies $g > \Gamma_{vib}, \Gamma_{cav}$, where Γ_{vib} and Γ_{cav} are the full-width at half-maximum (FWHM) of the vibrational and cavity modes, respectively. Therefore, the vibrational and the cavity modes (hereafter referred to as basis modes) hybridize and form new normal modes, denoted as upper, middle and lower polaritons (UP, MP and LP) (*17*, *19*, *23*) (Fig. 1b, bottom). Each polariton consists of a superposition of the basis modes. The polariton resonant frequency and composition, characterized by Hopfield coefficients, can be controlled by changing the incidence angle (Figs. 1c and 1d). For example, at 15° incidence angle, the UP consists of 59.4% $W(CO)_6$ carbonyl asymmetric stretch, 4.3% analogous vibration in $W(^{13}CO)_6$, and 36.3% cavity photon, while the LP is composed of 5.8%, 60.8%, and 33.4% of the respective basis modes. As discussed later, this information is essential to investigate the ability of strong coupling to mediate intermolecular VET.

We used two-dimensional infrared spectroscopy (2D IR) (*12–14*) to show VET from $W(CO)_6$ into $W(^{13}CO)_6$. In 2D IR, if the UP was pumped and VET occurred, a substantial population of $W(^{13}CO)_6$ excited states would be generated and the intensity of the corresponding cross peak would rise. In Fig. 2, we compare 2D IR spectra of the $W(CO)_6/W(^{13}CO)_6$ mixture inside and outside the microcavity. The 2D IR spectrum of the bare $W(CO)_6/W(^{13}CO)_6$ mixture (Fig. 2a) confirms the absence of energy transfer between vibrational modes. It shows two pairs of diagonal peaks, corresponding to excitations of asymmetric carbonyl modes of $W(CO)_6$ and $W(^{13}CO)_6$, respectively, whose vibrational lifetimes are c.a. 200 ps. There are no cross-peaks (dashed black box in Fig. 2a), indicating absence of intermolecular VET (SM Section 11).

The strongly coupled $W(CO)_6/W(^{13}CO)_6$ system provided a strikingly different picture. The 2D IR spectrum (Fig. 2b) shows several cross-peaks at t_2 = 30 ps, indicating cavity-induced intermolecular correlations. From previous studies (*12*, *15*), at t_2 = 30 ps (greater than the polariton lifetime), the remaining pumped energy equilibrates into the first excited state of dark modes. Furthermore, the $W(^{13}CO)_6$ dark modes have $v = 1 \rightarrow v = 2$ transitions at 1917 cm^{-1}, while those of $W(CO)_6$ are at 1961 cm^{-1}. Thus, the transient absorption at $\omega_3 = \omega_{LP}$ (~1920 cm^{-1}) and ω_{MP} (~1959 cm^{-1}) provide an optical window into population dynamics of the $W(^{13}CO)_6$ and $W(CO)_6$ reservoir modes, respectively (SM Section 13). In particular, the cross peak at $\omega_1 = \omega_{UP}$ and $\omega_3 = \omega_{LP}$ (denoted as $[\omega_{UP}, \omega_{LP}]$ hereafter; see red box in Fig. 2b) suggested that a larger fraction of the energy in UP (dominated by $W(CO)_6$) was transferred into the dark $W(^{13}CO)_6$ modes after 30 ps, a signature of intermolecular VET. We have also conducted 2D IR experiments with pump tailored to selectively excite |UP><UP| population states and a similarly strong cross peak appeared at $\omega_3 =$

Commented [FRR1]: Probably useful to have a reference for these claims.

Commented [BX2R1]: Below is the citation we find, but unfortunately we don't have enough space.

Arrivo, Steven M., et al. "Ultrafast infrared spectroscopy of vibrational CO-stretch up-pumping and relaxation dynamics of W (CO) 6." *Chemical physics letters* 235.3-4 (1995): 247-254.

ω_{LP} . Thus, the [ω_{UP}, ω_{LP}] and [ω_{UP}, ω_{MP}] cross-peaks (Fig. 2b) arise from UP population, whereas pump-driven coherences such as |UP><LP| and |UP><MP| provide no contribution to the observed spectral features (SM Section 5).

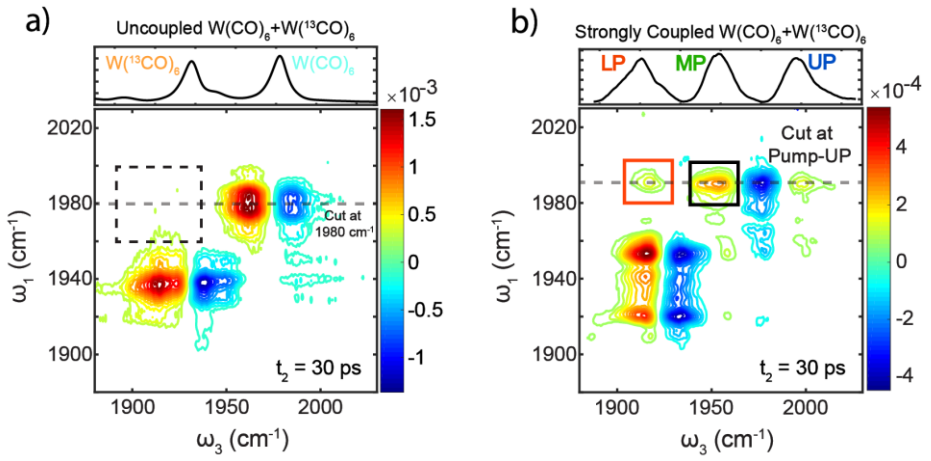

Fig. 2. 2D IR spectra of (a) uncoupled and (b) strongly coupled $W(CO)_6$/$W(^{13}CO)_6$ with a total of 105 mM concentrations in binary solvent (hexane-DCM), along with the corresponding linear spectra of the two systems (top panel in a and b). The strongly coupled sample is taken under an incidence angle of 15° (Fig. 1d) where the cavity resonance is kept at 1961 cm^{-1}.

We compared the cross-peak intensities at [ω_{UP},ω_{LP}] ($I_{UP,LP}$, red box in Fig. 2b) and [ω_{UP}, ω_{MP}] ($I_{UP,LP}$, black box in Fig. 2b) to determine the equilibrated excited-state populations of $W(^{13}CO)_6$ and $W(CO)_6$ (SM Section 12) arising from UP relaxation. Based on the Hopfield coefficients (for incidence angle of 15°), only 4.3% of the UP energy would be stored in $W(^{13}CO)_6$ reservoir modes, whereas 59.4% would be allocated to $W(CO)_6$ dark states. Therefore, in the absence of VET, the average population ratio between these reservoir modes ($I_{UP,MP}/I_{UP,LP}$) must be approximately equal to the ratio of the corresponding Hopfield coefficients, or 59.4%: 4.3% ≈ 14:1. However, experimentally, the $I_{UP,MP}/I_{UP,LP}$ ratio is 2.5:1. This observation suggested that after the UP population was optically generated, its energy was preferentially channeled into $W(^{13}CO)_6$, increasing relative peak intensity of [ω_{UP},ω_{LP}]. To further examine this argument, we conducted similar measurements with the cavity blue-detuned so that UP had a greater fraction of $W(CO)_6$ (SM. Section 7). Even at a Hopfield coefficient ratio of 25:1, there is still a significant amount of energy transfer ($I_{UP,MP}/I_{UP,LP}$ ratio to be 2.6±0.1). Additional evidence supports intermolecular VET is the anisotropy decay of [ω_{UP}, ω_{MP}] and [ω_{UP},ω_{LP}] peaks (see SM Section 8).

In Fig. 3a, we monitored the VET dynamics via pump-probe spectroscopy, when only |UP><UP| was excited, e.g. neither |LP><LP| nor any coherence states were pumped. The intensity of [ω_{UP},ω_{LP}] peak increased with a time constant of 5.7±0.6 ps. This value represents the timescale for energy transfer from UP into $W(^{13}CO)_6$ reservoir modes. In contrast, the direct relaxation of UP into $W(CO)_6$ happened much faster than VET with a lifetime of 1.5±0.3 ps, as indicated by the

rising dynamics of $I_{UP,MP}$. The decay of $I_{UP,MP}$ is composed of a fast and a slow component. The fast dynamics has a lifetime of 7±2 ps, similar to the rising time of $I_{UP,LP}$. Thus, it implies the initial energy 'leakage' from the $W(CO)_6$ mode into the $W(^{13}CO)_6$ mode (see SM Section 13). The slow component, whose decay extends beyond the time range of our scan, should correspond to the population relaxation of reservoir $W(CO)_6$ (*12*, *15*).

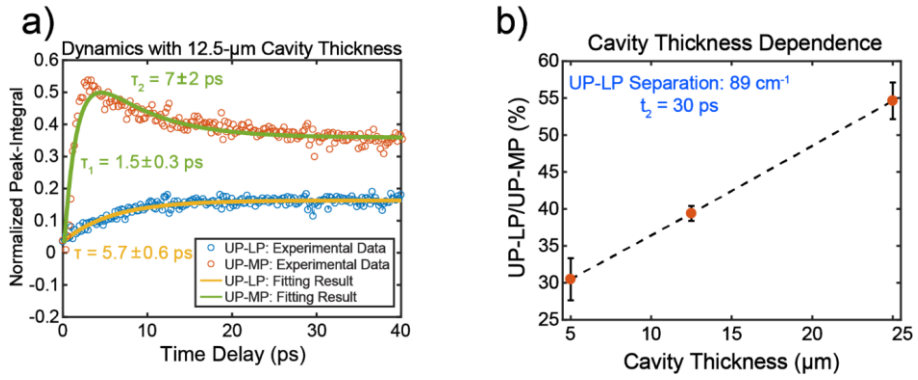

Fig. 3. (a) Dynamics of $[\omega_{UP},\omega_{LP}]$ and $[\omega_{UP},\omega_{UP}]$ peak integrals and the fitting results. The sample is taken under an incidence angle of 15° (Fig. 1d). (b) A plot of $I_{UP,MP}/I_{UP,LP}$ ratio as a function of cavity thickness at t_2 = 30 ps. The error bars are obtained from the standard deviation of three independent scans.

To confirm the importance of cavity modes in facilitating polariton VET, we attempted to enhance VET by increasing the cavity thickness *L*. In Fig. 3b, we present the $I_{UP,MP}/I_{UP,LP}$ ratio, for the same molecular mixture in cavities with *L* = 5, 12.5 and 25 μm, corresponding to 1.12, 2.80 and 5.60 ps cavity lifetimes, respectively (SM Section 4). This ratio, which reflects the efficiency of VET at 30 ps, increased with *L*. Because thicker cavities have longer lifetimes, this dependence suggested a larger fraction of UP energy was collected into $W(^{13}CO)_6$ modes as polariton decay by photon leakage became slower. This property substantiates that intermolecular VET involved polaritonic intermediate states (SM Section 13). The nature of the ultrafast energy redistribution process here requires further study, suggesting that, in contrast to measurements performed on organic microcavities (*17*, *19*), previously unexplored mechanisms should dominate the relaxation kinetics reported here. Possible mechanisms include polariton-to-polariton transitions, MP intraband relaxation, or participation of other dark modes.

The reported concept of polariton-enabled intermolecular VET could be expanded into the selective promotion or suppression of vibrational energy transport channels. The preferential relaxation into lower energy states is a key process for IR polariton condensation, remote energy transfer (*17*, *18*), and cavity chemistry (*22*, *24*).

References

1. D. C. Tardy, B. S. Rabinovitch, Intermolecular Vibrational Energy Transfer in Thermal Unimolecular Systems. *Chem. Rev.* **77**, 369–408 (1977).
2. J. P. Kraack, A. Frei, R. Alberto, P. Hamm, Ultrafast Vibrational Energy Transfer in Catalytic Monolayers at Solid-Liquid Interfaces. *J. Phys. Chem. Lett.* **8**, 2489–2495 (2017).
3. T. Baumann, M. Hauf, F. Schildhauer, K. B. Eberl, P. M. Durkin, E. Deniz, J. G. Löffler, C. G. Acevedo-Rocha, J. Jaric, B. M. Martins, H. Dobbek, J. Bredenbeck, N. Budisa, Site-Resolved Observation of Vibrational Energy Transfer Using a Genetically Encoded Ultrafast Heater. *Angew. Chemie - Int. Ed.* **58**, 2899–2903 (2019).
4. R. Gnanasekaran, J. K. Agbo, D. M. Leitner, Communication maps computed for homodimeric hemoglobin: Computational study of water-mediated energy transport in proteins. *J. Chem. Phys.* **135**, 065103 (2011).
5. D. J. Nesbitt, R. W. Field, Vibrational energy flow in highly excited molecules: Role of intramolecular vibrational redistribution. *J. Phys. Chem.* **100**, 12735–12756 (1996).
6. M. Gruebele, P. G. Wolynes, Vibrational Energy Flow and Chemical Reactions. *Acc. Chem. Res.* **37**, 261–267 (2004).
7. T. Förster, Intermolecular energy transfer and fluorescence. *Ann. Phys. (N. Y).* **437**, 55–75 (1948).
8. D. L. Dexter, A theory of sensitized luminescence in solids. *J. Chem. Phys.* **21**, 836–850 (1953).
9. R. F. Ribeiro, L. A. Martínez-Martínez, M. Du, J. Campos-Gonzalez-Angulo, J. Yuen-Zhou, Polariton chemistry: controlling molecular dynamics with optical cavities. *Chem. Sci.* **9**, 6325–6339 (2018).
10. H. Memmi, O. Benson, S. Sadofev, S. Kalusniak, Strong Coupling between Surface Plasmon Polaritons and Molecular Vibrations. *Phys. Rev. Lett.* **118**, 126802 (2017).
11. R. F. Ribeiro, A. D. Dunkelberger, B. Xiang, W. Xiong, B. S. Simpkins, J. C. Owrutsky, J. Yuen-Zhou, Theory for Nonlinear Spectroscopy of Vibrational Polaritons. *J. Phys. Chem. Lett.* **9**, 3766–3771 (2018).
12. B. Xiang, R. F. Ribeiro, A. D. Dunkelberger, J. Wang, Y. Li, B. S. Simpkins, J. C. Owrutsky, J. Yuen-Zhou, W. Xiong, Two-dimensional infrared spectroscopy of vibrational polaritons. *Proc. Natl. Acad. Sci. U. S. A.* **115**, 4845–4850 (2018).
13. B. Xiang, R. F. Ribeiro, L. Chen, J. Wang, M. Du, J. Yuen-Zhou, W. Xiong, State-Selective Polariton to Dark State Relaxation Dynamics. *J. Phys. Chem. A*. **123**, 5918–5927 (2019).

14. B. Xiang, R. F. Ribeiro, Y. Li, A. D. Dunkelberger, B. B. Simpkins, J. Yuen-Zhou, W. Xiong, Manipulating Optical Nonlinearities of Molecular Polaritons by Delocalization. *Sci. Adv.* **5**, eaax5196 (2019).

15. A. D. Dunkelberger, B. T. Spann, K. P. Fears, B. S. Simpkins, J. C. Owrutsky, Modified relaxation dynamics and coherent energy exchange in coupled vibration-cavity polaritons. *Nat. Commun.* **7**, 13504 (2016).

16. X. Liu, T. Galfsky, Z. Sun, F. Xia, E. C. Lin, Y. H. Lee, S. Kéna-Cohen, V. M. Menon, Strong light-matter coupling in two-dimensional atomic crystals. *Nat. Photonics*. **9**, 30–34 (2014).

17. X. Zhong, T. Chervy, L. Zhang, A. Thomas, J. George, C. Genet, J. A. Hutchison, T. W. Ebbesen, Energy Transfer between Spatially Separated Entangled Molecules. *Angew. Chemie - Int. Ed.* **56**, 9034–9038 (2017).

18. M. Du, L. A. Martínez-Martínez, R. F. Ribeiro, Z. Hu, V. M. Menon, J. Yuen-Zhou, Theory for polariton-assisted remote energy transfer. *Chem. Sci.* **9**, 6659–6669 (2018).

19. D. M. Coles, N. Somaschi, P. Michetti, C. Clark, P. G. Lagoudakis, P. G. Savvidis, D. G. Lidzey, Polariton-mediated energy transfer between organic dyes in a strongly coupled optical microcavity. *Nat. Mater.* **13**, 712–719 (2014).

20. X. Zhong, T. Chervy, S. Wang, J. George, A. Thomas, J. A. Hutchison, E. Devaux, C. Genet, T. W. Ebbesen, Non-radiative energy transfer mediated by hybrid light-matter states. *Angew. Chemie - Int. Ed.* **55**, 6202–6206 (2016).

21. K. Georgiou, P. Michetti, L. Gai, M. Cavazzini, Z. Shen, D. G. Lidzey, Control over Energy Transfer between Fluorescent BODIPY Dyes in a Strongly Coupled Microcavity. *ACS Photonics*. **5**, 258–266 (2018).

22. A. Thomas, L. Lethuillier-Karl, K. Nagarajan, R. M. A. Vergauwe, J. George, T. Chervy, A. Shalabney, E. Devaux, C. Genet, J. Moran, T. W. Ebbesen, Tilting a ground-state reactivity landscape by vibrational strong coupling. *Science (80-.).* **363**, 615–619 (2019).

23. M. Muallem, A. Palatnik, G. D. Nessim, Y. R. Tischler, Strong Light-Matter Coupling and Hybridization of Molecular Vibrations in a Low-Loss Infrared Microcavity. *J. Phys. Chem. Lett.* **7**, 2002–2008 (2016).

24. M. Du, R. F. Ribeiro, J. Yuen-Zhou, Remote Control of Chemistry in Optical Cavities. *Chem*. **5**, 1167–1181 (2019).

25. M. Khalil, N. Demirdöven, A. Tokmakoff, Coherent 2D IR Spectroscopy: Molecular Structure and Dynamics in Solution. *J. Phys. Chem. A*. **107**, 5258–5279 (2003).

26. P. Saurabh, S. Mukamel, Two-dimensional infrared spectroscopy of vibrational polaritons of molecules in an optical cavity. *J. Chem. Phys.* **144**, 124115 (2016).

27. D. V. Kurochkin, S. R. G. Naraharisetty, I. V. Rubtsov, A relaxation-assisted 2D IR spectroscopy method. *Proc. Natl. Acad. Sci. U. S. A.* **104**, 14209–14214 (2007).

28. M. Kowalewski, B. P. Fingerhut, K. E. Dorfman, K. Bennett, S. Mukamel, Simulating Coherent Multidimensional Spectroscopy of Nonadiabatic Molecular Processes: From the Infrared to the X-ray Regime. *Chem. Rev.* **117** (2017), pp. 12165–12226.

29. V. M. Agranovich, M. Litinskaia, D. G. Lidzey, Cavity polaritons in microcavities containing disordered organic semiconductors. *Phys. Rev. B*. **67**, 085311 (2003).

Acknowledgements. The authors thank Dr. Tyler Porter from Dr. Clifford Kubiak's group for his efforts in synthesizing the $W(^{13}CO)_6$ compounds. B.X. and W.X thank insightful discussion with Dr. Judy Kim on FRET. **Funding:** B.X. is supported by Roger Tsien Fellowship. B.X., L.C., J.W. and W. X. acknowledge the support from AFSOR YIP – FA9550-17-1-0094. Z.Y and W.X. thank the support by NSF CAREER DMR-1848215. The development of the kinetic model was carried out by M.D. and J.Y.-Z. under funding support from the US Department of Energy, Office of Science, Basic Energy Sciences, CPIMS Program under Early Career Research Program award DE-SC0019188. R.F.R. elucidated signatures of the energy transfer processes in the nonlinear spectra with funding from the Air Force Office of Scientific Research award FA9550-18-1-0289.
Author contributions: W. X. and J.Y-Z. conceived the original idea. W.X. supervised the overall research and J.Y-Z. supervised the theoretical work. B.X. and W.X. designed the experiments. B. X., L. C., Z. Y. and J. W. conducted the experimental work. B.X. and W.X. analyzed experimental data. R.F.R., M. D., and J.Y-Z developed theoretical work. B.X., R.F.R., M. D., J.Y-Z. and W. X interpreted and discussed the experimental and theoretical results and contributed to the writing of the final manuscript. **Competing interests:** Authors declare no competing interests. **Data and materials availability:** All data is available in the main text or the supplementary materials.

Supplementary Materials:

Materials and Methods

Supplementary Text

Figures S1-S19

Table S1-S2

References

Science
AAAS

Supplementary Materials for

Title: Intermolecular Vibrational Energy Transfer Enabled by Microcavity Strong Light-Matter Coupling

Bo Xiang[1], Raphael F. Ribeiro[2], Matthew Du[2], Liying Chen[2], Zimo Yang[1], Jiaxi Wang[2], Joel Yuen-Zhou[2,*], Wei Xiong[1,2,*]
*Correspondence to: joelyuen@ucsd.edu (Joel Yuen-Zhou) and w2xiong@ucsd.edu (Wei Xiong)

This PDF file includes:

Materials and Methods

Sample Preparation

The $W(CO)_6$ (Sigma-Aldrich) + $W(^{13}CO)_6$/cavity system is prepared in an IR spectral cell (Harrick) containing two dielectric CaF_2 mirrors with 96% reflectivity separated by a 5, 12.5 or 25-μm Teflon spacer and filled with $W(CO)_6$/(hexane+dichloromethane) solution where the volumetric ratio between hexane and dichloromethane (DCM) is 1:1. The ratio is optimized to reduce the spectral overlap between the $W(CO)_6$ and $W(^{13}CO)_6$ subsystems and thus suppress Förster energy transfer between these molecules outside the cavity while still maintaining significant energy gaps between polariton resonances.

Two-Dimensional Infrared Spectrometer

Two-dimensional infrared (2D IR) spectroscopy is applied to investigate the properties of the hybrid light-matter states of a $W(CO)_6$/ $W(^{13}CO)_6$/microcavity system. 2D IR is a 3rd order nonlinear coherent ultrafast spectroscopy that measures a two-point correlation function for vibrational modes and projects the frequencies of vibrational states at two-time incidences onto a 2D correlation map (*25–27*).

The setup scheme is shown in Fig. S1. 800-nm laser pulses (~35 fs, ~5 W, 1 kHz) generated by an ultrafast Ti:Sapphire regenerative amplifier (Astrella, Coherent) are sent into an optical parametric amplifier (OPA) (TOPAS, LightConversion) which outputs tunable near-IR pulses. The near-IR pulses are converted to mid-IR pulses through a difference frequency generation (DFG) process by a type II $AgGaS_2$ crystal (Eksma). After DFG, a CaF_2 wedge splits the mid-IR pulse into two parts: the 95% transmitted part is sent into a Ge-Acoustic Optical Modulator based mid-IR pulse shaper (QuickShape, PhaseTech) and is shaped into double pulses, which form the pump beam arm; the 5% reflected is the probe beam. Both pump (~ 1.1 μJ) and probe (~ 0.2 μJ) are focused by a parabolic mirror (f = 10 cm) and overlap spatially at the sample. The output signal is collimated by another parabolic mirror (f = 10 cm) and is upconverted to an 800-nm beam at a 5%Mg: $LiNbO_3$ crystal. The 800-nm beam that comes out of the OPA passes through an 800-nm pulse shaper which narrows its spectrum in the frequency domain (center wavelength of 791 nm and the FWHM of 0.5 nm or 9.5 cm^{-1}).

The pulse sequence is shown in Fig. S1. Two pump pulses and a probe pulse (pulse duration of 100~150 fs) interact with samples at delayed times (t_1, t_2, and t_3). After the first IR pulse, a vibrational coherence is generated, which is converted into a new state by the second IR pulse and is characterized by scanning t_1 (0 to 6000 fs with 20 fs steps) using the mid-IR pulse shaper. A rotating frame at f_0 = 1583 cm^{-1} is applied to shift the oscillation period to 80 fs and to make the scanning step meet the Nyquist frequency requirement. After waiting for t_2, the third IR pulse (probe) impinges on the sample, and the resulting macroscopic polarization emits an IR signal. This IR signal is upconverted by a narrow-band 800 nm beam. The upconversion process covers the t_3 time delay and the 800-nm pulse duration (full width at half maximum = 0.5 nm) determines the scanning length of t_3. The monochromator and CCD (Andor) experimentally Fourier transform the upconverted signal, thus generating a spectrum along the ω_3 axis. Numerical Fourier transform of the signal along the t_1 axis is required to obtain the spectrum along ω_1. The resulting 2D IR

spectra are plotted against ω_1 and ω_3. The t_2 time delay is scanned by a computerized delay stage which is controlled by home-written LabVIEW programs to characterize the dynamic features of the system. A rotational stage is mounted on the sample stage to choose the tilt angle and, therefore, the wavevector of the driven polaritons. One special requirement for this experiment is that the rotation axis of the stage needs to be parallel to the incidence plane formed by the pump and probe beams. In this way, we ensure that the in-plane wavevectors, $k_{||}$, of pump and probe pulses are the same. The particular $k_{||}$ value of the pump and probe beams are determined by checking the 1D transmission polariton spectra of the pump and probe pulses before and after 2D IR acquisitions.

Synthesis of $W(^{13}CO)_6$

$[Ph_3{=}N{=}Ph_3]Cl$ (Strem Chemicals) and ^{13}CO gas (Sigma-Aldrich) were utilized to synthesize $W(^{13}CO)_6$ starting from $W(CO)_6$. The precursor was prepared in the following reaction

$$W(CO)_6 + [Ph_3P = N = PPh_3]Cl \longrightarrow [Ph_3P = N = PPh_3][W(CO)_5Cl] + CO$$

The reaction took place in a Schlenk flask where the $W(CO)_6$ and $[Ph_3{=}N{=}Ph_3]Cl$ were mixed in 1.2-dimethoxyethane (DME). The reaction system was heated up to 85 °C and stirred for four hours. After being vacuumed to remove the CO gas, the products were vacuum-filtrated with a rinse of hexane. The $W(CO)_6$ residue was dissolved in hexane and rinsed down while the $[Ph_3P = N = PPh_3][W(CO)_5Cl]$ remained. After being dried by rotary evaporator, the oil-like $[Ph_3P = N = PPh_3][W(CO)_5Cl]$ became yellow powder and was ready for ^{13}CO-labeling.

The next step was to replace the [CO] groups with [^{13}CO]. The $[Ph_3P = N = PPh_3][W(CO)_5Cl]$ was dissolved in tetrahydrofuran (THF) under ^{13}CO atmosphere in Schlenk flask. The following reaction underwent for 24 hours with stirring at room temperature.

$$[Ph_3P = N = PPh_3][W(CO)_5Cl] + 5^{13}CO \longrightarrow [Ph_3P = N = PPh_3][W(^{13}CO)_5Cl] + 5CO$$

Before repeating the reaction, we got rid of the CO gas and filled in the ^{13}CO gas. The reaction system was frozen using liquid nitrogen in the vacuumization and refill cycles. This process was followed by the facilitated precipitation (see reaction below) with methanol where $W(^{13}CO)_6$ is not soluble. While the precipitation went on, the ^{13}CO was purged into the system. The purging and precipitation occurred for two days.

$$[Ph_3P = N = PPh_3][W(^{13}CO)_5Cl] + ^{13}CO \rightarrow [Ph_3P = N = PPh_3]Cl + W(^{13}CO)_6 \downarrow$$

By the end, the $W(^{13}CO)_6$ precipitate was filtered out and sublimated.

Supplementary Text

Section 1. FT IR Transmission Spectra of Uncoupled Two-Molecule System

Fig. S2 shows the FT IR spectrum along with Lorentzian fits for the lineshapes corresponding to each type of vibrational mode outside an optical cavity. Despite the small side peaks due to small impurities that barely influence the system, two main peaks are observed, located approximately at 1938 and 1982 cm^{-1}, respectively. The two absorption peaks have little spectral overlap, ensuring insignificant Förster energy transfer between the two molecular modes (see Section 10 for a detailed calculation).

We applied Lorentzian functions to fit the FT IR spectrum using

$$I_{Abs} = \sum_{i=1}^{2} \left[\frac{a_i \cdot c_i}{(x-b_i)^2 + (\frac{c_i}{2})^2} \right]. \quad \text{(S1)}$$

The parameters of the Lorentzians are given in Table S1. The Lorentzian fit for each molecule is employed later to compute the Förster energy transfer rate (Section 10).

Section 2. 2D IR of Uncoupled Molecular Systems

We further quantify the amount of VET in the following way. We first normalize 2D IR spectra by the linear transmission spectra of the polaritonic system to remove the spectral windowing effect (Fig. S3a) and then perform spectral cuts. Fig. S4a shows the normalized 2D IR spectral cuts at the ν_{01} mode (see Fig. 2a, dashed grey line) of $W(CO)_6$ (blue curve) and at $\omega_{pump} = \omega_{UP}$ (see Fig. 2b, dashed grey line) for the polariton system. By comparison, the uncoupled system shows insignificant cross-peak intensity around 1920 cm^{-1} (grey area), which indicates little energy transfer occurs between the two types of pure molecular modes, while in the strongly coupled systems, the UP-LP cross peak implies that energy transfer from UP state to $W(^{13}CO)_6$ mode is strong. To figure out the origin of the small bump observed at 1920 cm^{-1} for the bare system in the spectral cut (blue trace) at the $W(CO)_6$ fundamental frequency $\omega_1 = \omega_{01}$ (around 1980 cm^{-1}), we integrated the 2D IR spectra cut along ω_1 over a small region near $\omega_3 = 1920$ cm^{-1} for both coupled and uncoupled systems (shaded slices in Fig. S3a and S3b). The results are shown in Figs. S3c and S3d. Clearly, the 2D IR peak in the red box in Fig. S3a is in resonance with the UP-state around 1990 cm^{-1}, while the feature in the dashed black box is a result of the long tail of the $v = 1 \rightarrow v = 2$ transition of $W(^{13}CO)_6$.

To further prove that the referred cross-peak is due to a residue of $W(^{13}CO)_6$ $v = 1 \rightarrow v = 2$ transition response, a control experiment was performed where the two molecules ($W(CO)_6$ and $W(^{13}CO)_6$) were separated (with similar molecular concentration equivalent to 50% of the saturation concentration) and 2D IR scans were done for each case (Figs. S4b and S4c). By summing up the two 2D IR spectra, Fig. S4d was obtained. This figure shows the hypothetical 2D IR spectra which would be obtained if the transitions of each molecule type are completely uncorrelated, such that no energy transfer would happen in this scenario. By comparing the spectral cuts (Fig. S4e) at $\omega_1 = \omega_{01}$ (around 1980 cm^{-1}) of $W(CO)_6$ from all three 2D IR spectra (Figs. S4b-d), it is clear that the small feature at around 1920 cm^{-1} comes from the long tail of $W(^{13}CO)_6$ $v = 1 \rightarrow v = 2$ transition peak (red trace in Fig. S4e). The simple summation of the two 2D IR spectra

causes the misleading 'side-peak' (an orange trace in Fig. S4e), which is similar to the 'bump' in Fig. S4a. The spectral cut at ω_3 = 1920 cm^{-1} (Fig. S4f) further proves that there is no resonance around UP state of 1990 cm^{-1}, but just the end of the long tail of the $v = 1 \rightarrow v = 2$ transition of $W(^{13}CO)_6$ mode.

Section 3. Interpretation of 2D IR Features in Strongly Coupled Systems

Figs. S5a – d (*14*) show representative transient pump-probe spectra for the strongly coupled $W(CO)_6$ system measured at 15 degrees. In Fig. S5a, we present 1D transmission polariton spectra under pump-on and pump-off conditions, at t_2 = 5 ps (beyond cavity lifetime). When the pump is turned on, the UP resonance undergoes a shift towards a lower frequency (Fig. S5b), whereas the LP lineshape acquires a small positive shoulder that appears at a higher frequency and corresponds to a blue shift (Fig. S5d). These shifts are small but consistent and result in a derivative lineshape in the transient pump-probe spectrum (Fig. S5c). The peak-shift is induced by the Rabi splitting contraction which arises mainly due to the pump-induced reduction of the molecular ground-state population. The substantially reduced LP transmission upon pumping, and consequently the absorptive lineshape in the LP region of the pump-probe spectra, results from the dark mode $v = 1 \rightarrow v = 2$ transition (from first excited to second excited states, purple arrow in Fig. S5f) which is near-resonant with LP transition. As a result, ν_{12} becomes visible through the LP transmission window. Thus, when LP and ν_{12} are near resonance, the appearance of a strong absorptive transient signal at ω_{LP} is a signature of polariton relaxation the first excited state of the dark mode reservoir.

While pump-probe spectroscopy allows following polariton to dark state dynamics, the state-selective 2D IR spectrum (Fig. S5e) enables us to disentangle the dynamics (*11*, *12*): The UP-LP peak labeled in Fig. S5e (left-top) represents mainly the population transfer from UP into dark modes, while the LP-LP peak (Fig. S5e, left-bottom) arises primarily as a result of LP to dark mode population transfer and probe excited-state absorption by the reservoir. As summarized in Fig. S5f, polariton population transfer into dark modes occurs on a fast timescale. This process allows the reservoir transition ν_{12} to appear in the pump-probe or 2D spectra.

We learn the polariton relaxation dynamics by measuring the time-dependence of the LP peak in pump-probe spectra (via integration over the transient pump-probe peak near the LP position, e.g. the shaded area in Fig.S5c), and similarly, by measuring the dynamics of the UP-LP and LP-LP peaks from the 2D IR spectra (integrating the area corresponding to the 2D spectral peaks of UP-LP and LP-LP, e.g., the green boxes in Fig. S5e). We note that the exact integrated areas depend on the peak positions of various polariton systems.

In Fig. S5g, we show the 2D IR spectra obtained for the strongly-coupled two-molecule system at 15-deg incidence angle. For this system, three polaritonic states are formed. The UP model is mainly composed of the cavity and $W(CO)_6$ excited-states, while the LP state has significant components of cavity and $W(^{13}CO)_6$ polarization. Both molecular modes and the cavity field contribute significantly to the MP state. Based on the Hopfield coefficients shown in Fig. 1d (see also Section 11), most of the UP and a part of the MP features are induced by the strong coupling between the cavity and $W(CO)_6$ mode, which gives rise to the 2D IR features in the dashed black box in Fig. S5g. Conversely, strong coupling between cavity and $W(^{13}CO)_6$ mode is responsible for most of the LP and a part of those associated with MP, with the corresponding 2D IR responses

shown in the dashed red box in Fig. S5g. The overlap between these two sets of 2D IR 'sub-spectra' (shadowed area in Fig. S5g) shows the distortions of the 2D IR peaks relative to Fig. S5e, where only a single type of molecule is strongly coupled to the cavity. These distortions imply that the 2D IR spectra of the two-molecule system viewed is not equivalent to that obtained by merging the 2D IR spectra of two independent strongly-coupled systems. Nevertheless, the 2D IR features in both dashed red and black boxes are similar to those in Fig. S5e and they have similar origins as well. The peak in the green box is induced by the energy transfer from UP into $W(^{13}CO)_6$ dark modes and has been extensively discussed in the main text. A detailed theoretical discussion of the pump-probe spectra of the two-molecule system that supports this view is given in Section 12.

Section 4. Cavity-Thickness Dependence of 2D IR Spectra and Dynamics

Figure S6 shows the 2D IR spectra (a and b) and dynamics of UP-LP and UP-MP peak-integrals (c and d). From the fitting results, the rising component of polariton systems with 5, 12.5 and 25-μm cavity thicknesses, which indicates the energy transfer from UP state to $W(CO)_6$ reservoir modes occur with similar time scale. The decay component of them, on the other hand depends on the cavity-thickness, where the 25-μm system shows a slower energy leakage from $W(^{13}CO)_6$ via relaxation. Nevertheless, the systems of all different cavity thickness show qualitatively similar dynamical behaviors.

Section 5. 2D IR Spectra with $|UP\rangle\langle UP|$ and $|UP\rangle\langle LP|$ Narrow Pump

To check if the UP-LP cross-peak (green box in Fig. S5g) is indeed a result of energy transfer from an initial UP population into the dark reservoir or $W^{13}(CO)_6$ molecules, we performed additional experiments with narrow pumps. In Fig. S7a, we report the 2D IR spectra obtained when both pump pulses are narrowed such that they only overlap significantly the UP resonance (and thus only generate UP population), whereas in Fig. S7b, we show data obtained when the first pump pulse overlaps exclusively UP, while the second is only resonant with LP (thus, generating UP-LP coherences). From Fig. S7a, we can see that the UP-LP cross-peak is indeed indicative of biased energy transfer from UP into acceptor $W^{13}(CO)_6$ modes, i.e, the UP-LP/UP-MP peak ratio is larger than the ratio of UP Hopfield coefficient of $W^{13}(CO)_6$ to $W(CO)_6$ (40% vs. 4.3%). Conversely, the nonlinear signals reported in Fig. S7b is weak and dominated by noise, indicating that polariton coherence decay is not account for the larger than expected $W^{13}(CO)_6$ population reported in the 2D IR spectra with broadband pulses.

Section 6. Concentration Dependence of 2D IR Spectra

We have performed the concentration-dependent 2D IR experiments (Figure S8 a-c) on the strongly coupled system, where we fixed the t_2 time delay to be 30 ps and the cavity-thickness to be 12.5-micron. We calculate the ratio between UP-LP and UP-MP peak-integrals shown in Figure. S8c (red and black boxes). The peak ratio has a clear dependence on the molecular concentration which indicates the VET enabled by strong coupling is positively related to the coupling strength.

Section 7. Cavity-Detuning Dependence

Figure S9 shows the ratio between UP-LP and UP-MP peak integrals under different cavity-detuning conditions. We plotted a calibration line (red line along diagonal) as a boundary between

the scenario where energy transfer occurs and the case where only the energy redistribution happens for UP state. In the main text, we have kept the $W^{13}(CO)_6/W(CO)_6$ composition ratio in UP state to be 0.07. Here, we detune the cavity to vary the composition ratio. From the plot above, we found that the ratios of UP-LP/UP-MP, which indicates the population between excited acceptors and donors, have a very weak dependence on the detuning. In particular, we found even under conditions where the $W^{13}(CO)_6/W(CO)_6$ composition ratio of UP state is dropped to 0.04, there is still a large population of $W^{13}(CO)_6$ (acceptor) being excited.

Section 8. Anisotropy of Uncoupled and Strongly Coupled Systems

To further examine the nature of UP-LP and UP-MP cross-peak dynamics in strong coupling 2D IR spectra, we performed anisotropy measurements of UP-pump transient pump-probe scans on the strongly coupled system. The anisotropy is calculated by peak-intensity of pump-probe scans, under the parallel and perpendicular polarization combinations.

$$Anisotropy = \frac{I_{parallel} - I_{perpendicular}}{I_{parallel} + 2I_{perpendicular}}. \quad \text{(S2)}$$

Figure S10 shows the anisotropy decay of the bare $W(CO)_6$ molecular system, UP-LP and UP-MP cross-peaks in the strong coupling system. By comparison, the UP-MP has an anisotropy decay trend (lifetime of 3±1 ps) similar to the one of the bare molecular system (lifetime of 5±2 ps), while the UP-LP peak has nearly no significant anisotropy. This result suggests that the UP-MP peak represents population relaxation from UP to $W(CO)_6$, which preserves the original orientation of UP, followed by anisotropy decay. On the other hand, the UP-LP peak represents intermolecular vibrational energy transfer from UP (or $W(CO)_6$) to $W(^{13}CO)_6$, which loses the orientation correlation to the initial excitation. The results of the anisotropy investigation further support that the UP-LP cross-peak is a signature of intermolecular VET.

Commented [xw3]: Cite Bakker's paper

Commented [BX4R3]: Woutersen, Sander, and Huib J. Bakker. "Resonant intermolecular transfer of vibrational energy in liquid water." *Nature* 402.6761 (1999): 507-509.

Section 9. Relevant Feynman Diagrams

Relevant Feynman diagrams are shown in Fig. S11 (top panel). The pathways of energy transfer and relaxation between polaritonic modes and donor or acceptor modes are listed (*28*). We performed the Gaussian fitting to 2D IR spectral cuts at pump-LP, pump-MP and pump-UP states,respectively (Fig. S11, bottom panel). Five Gaussian components are identified, four of which correspond to specific Feynman diagrams (see the labels in Fig. S11). The fifth one of all the fitting curves represents the contribution from Rabi splitting contraction (*12*, *15*).

Section 10. Förster Energy Transfer Rate

Fluorescence resonance energy transfer (FRET) is the process by which excited molecules (donors) transfer energy to weakly-coupled acceptor species. The FRET rate is mainly determined by the donor-acceptor (D-A) distance, spectral overlap and transition dipole moments of each molecule. In this work, $W(CO)_6$ and $W(^{13}CO)_6$ form a D-A pair. The former emits around 1982 cm^{-1} with 9.15 cm^{-1} bandwidth, while the absorption of the latter centered at 1938 cm^{-1} and its bandwidth is of 10.53 cm^{-1} (see Section 1).

The FRET efficiency is given by the equation below

$$E_{FRET} = \frac{R_0^6}{R_0^6 + r^6}, \qquad \text{(S3)}$$

where r is the intermolecular distance that can be estimated as $1/\sqrt[3]{c_0 N_A}$, c_0 is the molecular concentration (105.26×10^{-3} mol/L) and N_A is Avogadro's number (6.022×10^{23} /mol). Hence, r = 2.64 nm. The quantity R_0 is denoted the Förster distance. It is expressed as

$$R_0 = \sqrt[6]{3 \times \frac{9000(\ln 10)\kappa^2 Q_D}{128\,\pi^5 N_A n^4} J(\lambda)}, \qquad \text{(S4)}$$

where κ^2 is a factor representing the dipolar orientation of the molecular system, here assumed to be 2/3 (the appropriate result for a randomly-oriented system), n is the optical refractive index (roughly 1.4 for most solvents, including hexane and DCM), and Q_D is the donor ($W(CO)_6$) quantum yield in the absence of acceptor ($W(^{13}CO)_6$)

$$Q_D = \frac{1}{1 + \tau_{rad}/\tau_{nonrad}}, \qquad \text{(S5)}$$

where τ_{rad} is the radiative decay lifetime of the donor and τ_{nonrad} is its nonradiative lifetime in the absence of acceptor molecules. The latter quantity can be obtained by performing a transient pump-probe experiment of the uncoupled donor system (see results in Fig. S12). The dynamic trace of the donor mode is shown in Fig. S9b. From the single exponential fit, we find the donor τ_{nonrad} is equal to 200 ± 4 ps.

The donor radiative lifetime is given by

$$\tau_{rad} = \frac{3\varepsilon_0 h c^3}{16\pi^3 |\mu_{01}|^2 n \nu^3}, \qquad \text{(S6)}$$

where $|\mu_{01}|$ is the effective transition dipole moment of $W(CO)_6$ (~ 1 Debye), ε_0 is the vacuum permittivity (8.85×10^{-12} $C^2/(N\cdot m^2)$), h is Planck's constant (6.626×10^{-34} $m^2\cdot kg/s$), c is the speed of light (2.998×10^8 m/s), n is the refractive index (~1.4) and ν is the frequency of the donor mode (1982 cm^{-1}). It follows that τ_{rad} and Q_D, are equal to 2.87×10^{-4} s and 7.0×10^{-7}, respectively.

The quantity $J(\lambda)$ is the normalized spectral overlap integral. It can be calculated from the emission spectrum of the donor, and the absorption spectrum of the acceptor:

$$J(\lambda) = \frac{\int_0^\infty F_D(\lambda)\varepsilon_A(\lambda)\lambda^4 d\lambda}{\int_0^\infty F_D(\lambda)d\lambda}, \qquad \text{(S7)}$$

where λ is the wavelength, $F_D(\lambda)$ the corrected fluorescence intensity of donor modes (in the absence of fluorescence data, we used the absorption intensity), and $\varepsilon_A(\lambda)$ is the frequency-dependent extinction coefficient of the acceptor mode. These functions are estimated with the Lorentzian fits obtained for the D-A system absorption spectrum (see Section 1). It follows that $J(\lambda)$ is 6.64×10^{16} $M^{-1}\cdot cm^{-1}\cdot nm^4$.

From these results, we obtain the following quantitative estimates for the Förster distance and FRET efficiency:

$$R_0 = 0.0211[\kappa^2 n^{-4} Q_D J(\lambda)]^{1/6}\ (nm) = 1.135\ (nm), \qquad \text{(S8)}$$

$$E_{FRET} = \frac{R_0^6}{R_0^6 + r^6} = \frac{1.135^6}{1.135^6 + 2.64^6} = 0.63\%. \qquad \text{(S9)}$$

Section 11. Hopfield Coefficients

The compositions of each basis mode for different polaritonic states can be calculated based on fits of the experimentally obtained dispersive curves (Fig. 1c). The Hopfield coefficient equation for a three-component strongly-coupled system is

$$\begin{pmatrix} E_{cav} & g_1 & g_2 \\ g_1 & E_{vib1} & 0 \\ g_2 & 0 & E_{vib2} \end{pmatrix} \begin{pmatrix} \alpha_{cav} \\ \alpha_{vib1} \\ \alpha_{vib2} \end{pmatrix} = E \begin{pmatrix} \alpha_{cav} \\ \alpha_{vib1} \\ \alpha_{vib2} \end{pmatrix}, \qquad \text{(S10)}$$

where E_{cav}, E_{vib1} and E_{vib2} are the energies of cavity mode, fundamental modes of $W(CO)_6$ (vib1) and $W(^{13}CO)_6$ (vib2), and g_1 and g_2 correspond to the coupling strengths between cavity mode and the $W(CO)_6$ and $W(^{13}CO)_6$ modes, respectively. The coupling between two molecular vibrational modes is considered as negligible, thus leading to zero molecular cross-terms in the Hamiltonian matrix. The compositions, or fractions, of each basis in a polariton state α is given by $|\alpha_{cav}|^2$, $|\alpha_{vib1}|^2$ and $|\alpha_{vib2}|^2$.

First, the eigenvalues (energies of LP, MP and UP states) are obtained by solving the secular equation

$$det\begin{pmatrix} E_{cav} - E & g_1 & g_2 \\ g_1 & E_{vib1} - E & 0 \\ g_2 & 0 & E_{vib2} - E \end{pmatrix} = 0. \qquad \text{(S11)}$$

In this work, E_{vib1} and E_{vib2} are 1982 and 1938 cm^{-1}; both g_1 and g_2 are estimated to be 23 cm^{-1} in the hexane-DCM mixture. The variable E_{cav} is the only parameter that is varied, as it is determined by the incident angle. By comparing the calculated LP, MP and UP energies to the experimental spectra (shown in Fig. 1c), we fit E_{cav} using the minimizing unsigned error condition

$$\sum [E_i(cal) - E_i(exp)]^2 \rightarrow min, \qquad \text{(S12)}$$

where i = LP, MP or UP. The fitted dispersive curves are shown in Fig. S13 (dashed green curves). Following the calculation of eigenvalues, the Hopfield coefficients $|\alpha_{cav}|^2$, $|\alpha_{vib1}|^2$ and $|\alpha_{vib2}|^2$ can be easily obtained and plotted as a function of incident angle (Fig. 1d).

Section 12. Pump-Probe Transmission

In this section, we provide the generalization of the mean-field theory constructed to describe polariton nonlinear response, which allows a description of the pump-probe response of the two-molecule system in terms of the incoherent reservoir (dark) population of each type of molecule. This generalization is necessary as it allows us to correlate experimentally observed cross-peak intensities with the fraction of excited donor and acceptor molecules.

The procedure we will follow is essentially equal to our previous work (*11*), except that our system now contains two sources of molecular polarization with different resonance frequencies. Given the similarity in derivation with previously published results, we present only the final expression for the differential (pump-probe) transmission spectrum. For additional details, we refer the reader to our previous work (*11*).

Let f_{pu}^{α} denote the fraction of molecules of type α (where α = D or A, corresponding to $W(CO)_6$ and $W^{13}(CO)_6$ molecules, respectively) in the first excited-state at a pump-probe delay time t_{PP}. The self-heterodyned third-order signal measured via differential pump-probe transmission is obtained from:

$$\Delta T^{pp} = T^{pp} - T^{(1)}, \qquad \text{(S13)}$$

where T^{pp} is the nonlinear probe transmission (after pumping) and $T^{(1)}$ is the probe linear transmission (in the absence of any pumping). By extending the pump-probe response model (*11*) to the present situation, we find that, to leading-order in the excited-state populations f_{pu}^{α} (or equivalently, in the pump field intensity),

$$\frac{\Delta T^{pp}(\omega)}{T^{(1)}(\omega)} = -2\mathrm{Re}\left[\frac{f_{pu}^{D}\dfrac{4\Delta_D\, g_D^2\, N_D}{\omega-(\omega_D-2\Delta_D)+i\frac{3\gamma_D}{2}} + f_{pu}^{A}\dfrac{4\Delta_A\, g_A^2\, N_A}{\omega-(\omega_A-2\Delta_A)+i\frac{3\gamma_A}{2}}}{\left(\omega-\omega_c+i\frac{\kappa}{2}\right)\left(\omega-\omega_D+i\frac{\gamma_D}{2}\right)\left(\omega-\omega_A+i\frac{\gamma_A}{2}\right)-g_D^2N_D-g_A^2N_A}\right] \qquad \text{(S14)}$$

where ω_c is the cavity-mode frequency, κ is its decay rate, and $\omega_\alpha, g_\alpha, \Delta_\alpha, N_\alpha$, and γ_α are the bare fundamental frequency, single-molecule light-matter coupling, anharmonic shift, the total number and homogeneous linewidth of the molecules of type α, respectively.

As expected, when the pump is sufficiently weak, the normalized differential pump-probe transmission spectrum is directly proportional to the populations of excited donor and acceptor molecules, which is defined as $N_{pu}^{D} = f_{pu}^{D} * N_D$, and $N_{pu}^{A} = f_{pu}^{A} * N_A$, respectively.

From our expression for the nonlinear transmission (Eq. S14), we can see that the pump-probe response will be larger when the polaritons are near-resonant with either of the available (excited-state absorption) overtone transitions, $\omega_D - 2\Delta_D$ of the donor or $\omega_A - 2\Delta_A$ of the acceptor. For the system discussed in this study, the overtones of donor and acceptor are resonant with MP and LP, respectively. When ω is approximately equal to $\omega_{MP} \approx \omega_D - 2\Delta_D$, the spectral feature is only

significantly dependent on the population of the excited donor, N_{pu}^{D}, i.e., it has little dependence on the excited-state acceptor population, N_{pu}^{A}. Similarly, this is true when we take ω approximately equal to $\omega_{LP} \approx \omega_A - 2\Delta_A$, i.e., the spectral feature measured in pump-probe at LP is very weakly dependent on the fraction of donor excited-state, N_{pu}^{D}.

In Fig. S14, we provide numerical evidence of these statements by illustrating the relationship between the ratio of acceptor to donor excited-state population, N_{pu}^{A}/N_{pu}^{D} and the normalized ratio of the area under the LP peak [defined as the integral of $-\Delta T^{pp}(\omega)/T^{(1)}(\omega_{LP})$ within an interval of FWHM = 10 cm^{-1} centered at ω_{LP}] to that of the similarly defined MP peak area. To mimic the experimental conditions, we keep the molar ratio of acceptor to the donor, N_A/N_D, equal to 1, and choose the collective light-matter coupling $g_D\sqrt{N_D} = g_A\sqrt{N_A}$ = 20 cm^{-1}. All other parameters are obtained from the spectra of the bare molecules or cavity. Each of the plotted curves correspond to a fixed donor excited-state population, f_{pu}^{D}, which varies between 0.5% and 4%.

Note that the LP to MP ratios are consistently correlated to the acceptor to donor excited-state population ratios with a slight overestimation of the latter by a factor that ranges from 1.2 to 1.4. For example, when $f_{pu}^{D} = 0.01\%$ and $N_{pu}^{A}/N_{pu}^{D} = 30\%$, our model predicts the slightly larger ratio of 42% for the ratio of the LP to MP peak ratios. The discrepancy becomes worst when N_{pu}^{A}/N_{pu}^{D} are increased, e.g., when $f_{pu}^{D} = 0.01$ and $N_{pu}^{A}/N_{pu}^{D} = 50\%$, our model predicts a 71% LP to MP ratio. The difference between N_{pu}^{A}/N_{pu}^{D} and the peak intensity ratios increase with larger acceptor or donor excited-state populations because the approximation that the transient LP and MP transmission depend only on the excited-state population of the molecule with corresponding resonant overtone transition becomes worse. This can be seen from Eq. S14, which shows that the nonlinear response at any given frequency is determined by contributions from both N_{pu}^{A} and N_{pu}^{D}. Nevertheless, with this relationship, we can estimate the population ratio of the excited acceptor to the excited donor with reasonable accuracy. For example, in our experiment (with cavity length *12.5-μm* and concentration of 105.26×10^{-3} mol/L), we observed an approximate LP/MP ratio of 30%, which allows us to conclude that N_{pu}^{A}/N_{pu}^{D} is between 25% and 35% which is still way significant than the acceptor to donor UP-Hopfield coefficient ratio.

For the sake of completeness, we also present in Fig. S15, a plot of $-\Delta T^{pp}(\omega)$ for a donor excited-state population fraction of 4% and acceptor varying from 0.4% to 2%. The observed features agree well with the experiment.

Section 13. Kinetic Model for Energy Transfer Dynamics

To gain insight into the dynamics measured by 2D IR, we carry out phenomenological kinetic modeling. The dynamic traces (Figs. 3a, S6c-d) suggest that an excited UP state transfers energy to the W(CO)$_6$ dark states (D), which then transfer energy to the W(^{13}CO)$_6$ dark states (A). The latter process seems to occur via polaritonic intermediate states, based on the dependence of VET on cavity length (Fig. 3b) and thus cavity lifetime. Possible intermediates include the MP states, whose energies lie between those of D and A. Motivated by these ideas, we consider a simple model for population (ρ) exchange among an excited UP state with in-plane wavevector q (U$_q$), D, all MP states (M), and A:

$$\frac{d\rho_{U_q}}{dt} = -\left[f_{U_qD}k_1 + f_{U_qA}k_1 + f_{U_qD}\gamma_D + f_{U_qA}\gamma_A + f_{U_qC}\kappa\right]\rho_{U_q} \tag{S15}$$

$$\frac{d\rho_D}{dt} = -[d_M f_{MD}k_2 + \gamma_D]\rho_D + f_{U_qD}k_1\rho_{U_q} + \tilde{f}_{MD}k_1\rho_M \tag{S16}$$

$$\frac{d\rho_M}{dt} = -\left[\tilde{f}_{MD}k_1 + f_{MA}k_1 + f_{MD}\gamma_D + f_{MA}\gamma_A + f_{MC}\kappa\right]\rho_M + d_M f_{MD}k_2\rho_D + d_M\tilde{f}_{MA}k_3\rho_A \tag{S17}$$

$$\frac{d\rho_A}{dt} = -[d_M\tilde{f}_{MA}k_3 + \gamma_A]\rho_A + f_{U_qA}k_1\rho_{U_q} + f_{MA}k_1\rho_M \tag{S18}$$

Rate constants for transitions are denoted by k, and those for decay inherent to the (uncoupled) basis modes are given by γ (vibrational damping) and κ (cavity leakage). In particular, k_1^{-1} is a characteristic timescale for relaxation from polariton to dark states, while k_2 and k_3 are associated with the reverse process. Transitions not captured by Eqs. (S15)-(S18), including those involving LP states, are taken to be negligible.

The compositions (or Hopfield coefficients) of $W(CO)_6$, $W(^{13}CO)_6$, and cavity photon in polariton manifold $\alpha = U_q, M$ are given by $f_{\alpha D}$, $f_{\alpha A}$, and $f_{\alpha C}$, respectively. Each f_{MX} $(X = D, A, C)$ is the average value over the entire range of MP states: $f_{MX} = \langle f_{M_qX}\rangle$, where f_{M_qX} is the corresponding composition for the MP state with in-plane wavevector q (MP_q). Explicitly, the average is expressed as $\langle\cdot\rangle = \sum_{q=0}^{q_{max}^{(M)}} q(\cdot) \,/\, \sum_{q=0}^{q_{max}^{(M)}} q$. The density of states dN/dq is (up to a constant) represented in each summand by q, and $q_{max}^{(M)}$ is the maximum wavevector of the MP band. Here, we define $q_{max}^{(M)}$ as q satisfying $E_{M_q} + \frac{\Gamma_{M_q}}{2} = E_D - \frac{\Gamma_D}{2}$, where E denotes energy, Γ indicates spectral linewidth, and $\Gamma_{M_q} = f_{M_qD}\Gamma_D + f_{M_qA}\Gamma_A + f_{M_qC}\kappa$ is that of MP_q. This heuristic criterion says that the MP band is ill-defined at wavevectors where it significantly overlaps in energy with D; a similar criterion based on wavevector broadening is discussed in (*29*). Another quantity dependent on $q_{max}^{(M)}$ is the ratio $d_M = \sum_{q=0}^{q_{max}^{(M)}} q \,/\, \sum_{q=0}^{q_{max,R}^{(M)}} q$, which compares the number of states in the MP band to that of a "reference setup" (see below) with maximum MP wavevector $q_{max,R}^{(M)}$. In accordance with Fermi's golden rule, d_M in Eqs. (S16)-(S18) ensures that the rate of energy transfer into MP scales with the number of states in the polariton manifold. Assuming energy exchange is mediated by a bath at thermal equilibrium, the "effective Hopfield coefficients" $\tilde{f}_{MD} = \langle f_{M_qD}\exp[(E_D - E_{M_q})/k_BT]\rangle$ and $\tilde{f}_{MA} = \langle f_{M_qA}\exp[(E_{M_q} - E_A)/k_BT]\rangle$ become relevant when describing energetically uphill transitions M → D and A → M, respectively. k_B is the Boltzmann constant, and T is the temperature.

Polariton energies and compositions are computed by diagonalizing the Hamiltonian for the strongly coupled system (see Section 11). For cavity dispersion and strength of light-matter coupling to each molecular species, we respectively use standard expressions $E_{cav}(q) =$

$\frac{\hbar c}{n}\sqrt{q^2+\left(\frac{m\pi}{L}\right)^2}$ and $g(q)=\sqrt{C}\mu\sqrt{\frac{E(q,m)}{2n^2\epsilon_0}}$, where $\hbar$ is the reduced Planck's constant, c is the speed of light in vacuum, and ϵ_0 is the vacuum permittivity. For a given cavity mode, the dispersion and light-matter coupling depend on the mode order m, as well as the refractive index n and the length L of the cavity. E_{cav} and g also depend on the concentration C and transition dipole moment μ of the carbonyl asymmetric stretch modes. In the calculations below, we consider only the m = 5 cavity mode and suppose $W(CO)_6$ and $W(^{13}CO)_6$ have identical concentrations and transition dipole moments.

To simulate population dynamics, we parameterize the above kinetic model. The parameters are reported in Table S2 and constitute the "reference setup". A number of values are taken directly from the experiments in this work or are well-accepted in the literature. Other values (i.e., L, μ) are chosen so that the calculated polariton dispersion (Fig. S16a) and Hopfield coefficients (Fig. S16b) agree well with experimental results (Figs. 1c-d). Also, note that k_1 is consistent with previous measurements showing that polaritons relax into dark states in < 5 ps (*13*).

We now compare the dynamics observed using 2D IR with simulated dynamics. As explained in the main text, relative populations of D and A are represented in the experiments by the UP-MP and UP-LP peak integrals, respectively. Comparing the measured peak integrals (Fig. 3a) to the corresponding calculated populations (Fig. 17a), we find good qualitative agreement. In addition, both experiment and theory demonstrate that the relative populations of D and A at t_2 = 30 ps are essentially independent of which UP state is initially excited (compare Fig. S9 with Fig. S17b). We also simulate VET for different cavity lifetimes (Fig. S18a) and concentrations of the strongly coupled molecular species (Fig. S18b). Again, qualitative resemblance—namely, in the sign of the correlation—is found when comparing the calculations with experiments varying cavity length (Fig. 3b), which is proportional to cavity lifetime, and concentration (Fig. S8d).

Overall, the presented kinetic model not only predicts polariton-assisted intermolecular VET, but even captures major qualitative features of the phenomenon. The theory supports the following VET mechanism (Fig. S19). The initially excited UP, which is mostly composed of $W(CO)_6$, relaxes quickly, irreversibly, and almost exclusively into D. From D, energy is transferred to states all throughout the MP band. MP subsequently undergoes fast relaxation into A. While the reverse processes can occur, the forward transitions are sufficiently rapid to afford relative populations of D and A exceeding those predicted based on the Hopfield coefficients of the initially excited UP state.

However, discrepancies between experiments and theory raise a conundrum regarding MP as a VET intermediate (Fig. S19). Unlike the measured D and A populations (Fig. 3a), the corresponding simulated quantities (Fig. S17a) are still decaying after 40 ps. This relaxation is primarily attributed to the decay of MP due to cavity leakage. Moreover, the modeling predicts that the increase of ρ_A/ρ_D (after 30 ps) with cavity lifetime (Fig. S18a) and concentration (Fig. S18b) shifts from linear to sublinear above certain values of the varied parameters. No such trend is measured experimentally within the same parameter ranges (Figs. 3b and S8d). In the

calculations, higher concentrations lead to lower cavity composition in MP, producing the same effect as longer cavity lifetimes: reduced damping of MP. These contrasts indicate that, if MP indeed facilitates energy transfer from D to A, then MP decays differently than expected from cavity linewidth and Hopfield coefficients.

That MP can mediate VET between D and A is also puzzling in light of conventional understanding of polariton relaxation. Typically, polariton relaxation is mediated by the interaction of the strongly coupled molecular modes with solvent or other intramolecular degrees of freedom. According to existing theories for this mechanism (*18*, *29*), we expect transitions to polariton states to be several orders of magnitude slower than transitions to dark states; this large difference stems from the small fraction of total states that are polariton states. Thus, the seemingly fast relaxation from D or A to MP (Fig. S19) posts new challenges to the existing theories.

The perplexing VET dynamics might be explained by other mechanisms. One example is the involvement of dark intermediate states(*13*), which make up a larger number of total states and likely have longer lifetimes compared to MP. Another alternative is that the MP serves as an intermediate for scattering from D to A. This idea would resolve the issue of unexpectedly long lifetimes while providing the potential for supertransfer enhancement due to the delocalization of MP.

Commented [BX5]: Lloyd, Seth, and Masoud Mohseni. "Symmetry-enhanced supertransfer of delocalized quantum states." *New journal of Physics* 12.7 (2010): 075020.

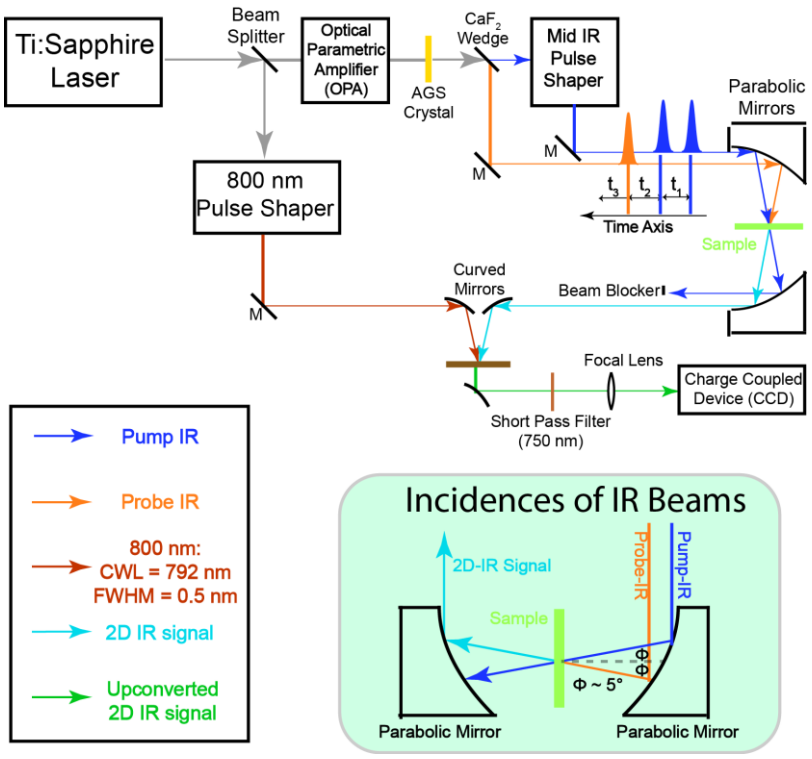

Fig. S1.
Scheme of two-dimensional infrared experimental setup. The inset shows the incidence of pump and probe IR beams.

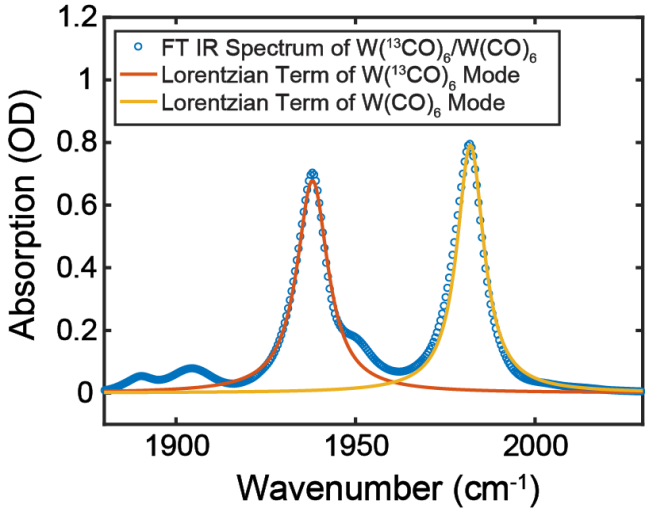

Fig. S2.
Linear FT IR spectrum of uncoupled two-molecule system. Lorentzian fits for the asymmetric stretch mode of each type of molecule.

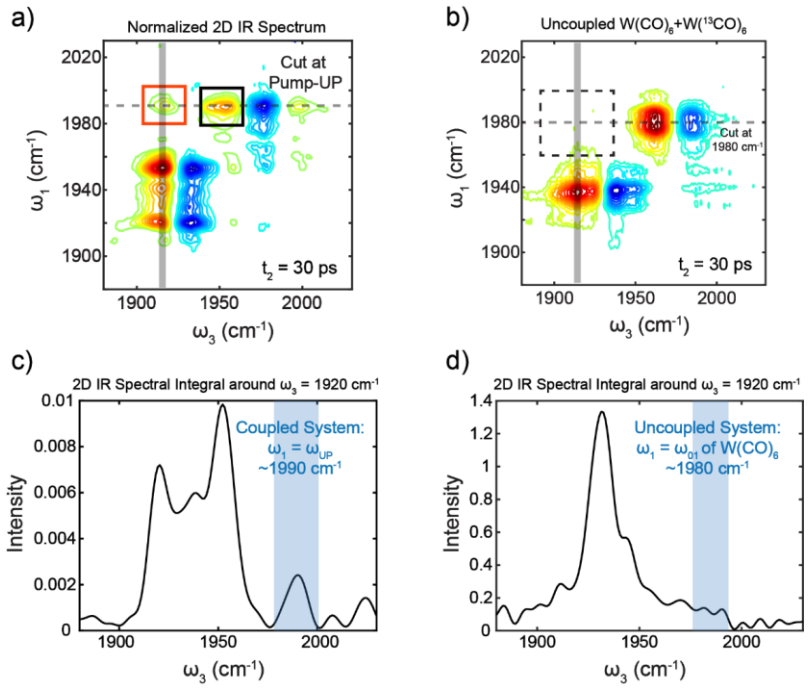

Fig. S3.
2D IR spectra. (a) strongly coupled (cavity with longitudinal length of 12.5 μm) and (b) uncoupled $W(CO)_6 + W(^{13}CO)_6$ systems. 2D IR spectral cut at $\omega_3 = \omega_{LP}$ around 1920 cm^{-1} of (c) strongly coupled and (d) uncoupled $W(^{13}CO)_6 + W(CO)_6$ systems, showing the 2D IR peak in the red box corresponds to a specific transition, while the small feature in dashed black box in b is due to the tail of the $W(^{13}CO)_6$ 1→2 transition lineshape.

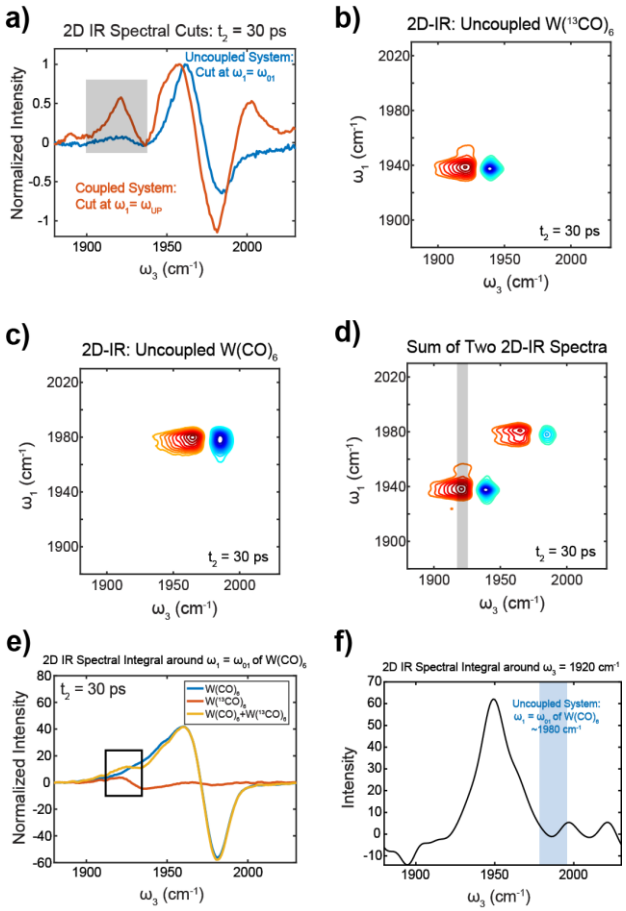

Fig. S4.

2D IR of uncoupled molecular systems. (a) 2D IR spectral cuts at the ν_{01} mode (see Fig. 2a, dashed grey line) of $W(CO)_6$ (blue curve) and at $\omega_{pump} = \omega_{UP}$ (see Fig. 2b, dashed grey line) for polariton systems with cavity longitudinal lengths of 12.5-μm (red curve) at $t_2 = 30$ ps. The spectral cuts are normalized to the peak around 1960 cm^{-1}. 2D IR spectra of (b) uncoupled $W(^{13}CO)_6$ system and (c) uncoupled $W(CO)_6$ system. (d) Sum of 2D IR spectra of both bare molecular systems. (e) 2D IR spectral cut at $\omega_1 = \omega_{01}$ of $W(CO)_6$ around 1980 cm^{-1} for all three 2D IR spectra (b, c and d). (f) 2D IR spectral cut at $\omega_3 = \omega_{12}$ of $W(^{13}CO)_6$ (around 1920 cm^{-1}) given by the spectra obtained from the linear combination of the 2D IR spectra of both bare molecular systems (grey slice in d).

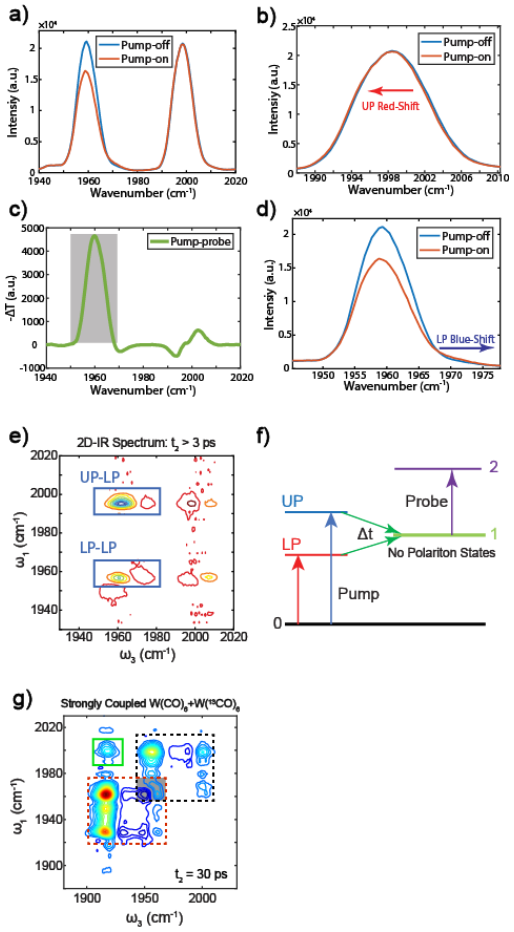

Fig. S5.

Pump probe and 2D IR spectra of molecular polaritons. a) Pump-on and pump-off spectra of strongly coupled $W(CO)_6$/hexane system with cavity longitudinal lengths of 12.5-μm in transient pump-probe experiment at t_2 =5 ps with roughly 15-deg incidence angle and saturated concentration; b) UP branch zoom-in; c) pump-probe spectrum at t_2 = 5 ps; d) LP branch zoom-in; (e) 2D IR spectrum of strongly coupled $W(CO)_6$/hexane system at t_2 = 5 ps; (f) Schematic illustration of the population transfer process when the polariton system is in equilibrium (t_2 = 5 ps). (g) 2D IR spectrum of strongly coupled $W(CO)_6$/$W(^{13}CO)_6$ with roughly 15-deg incidence angle and saturated concentrations in binary solvent (hexane-DCM) at t_2 = 5 ps.

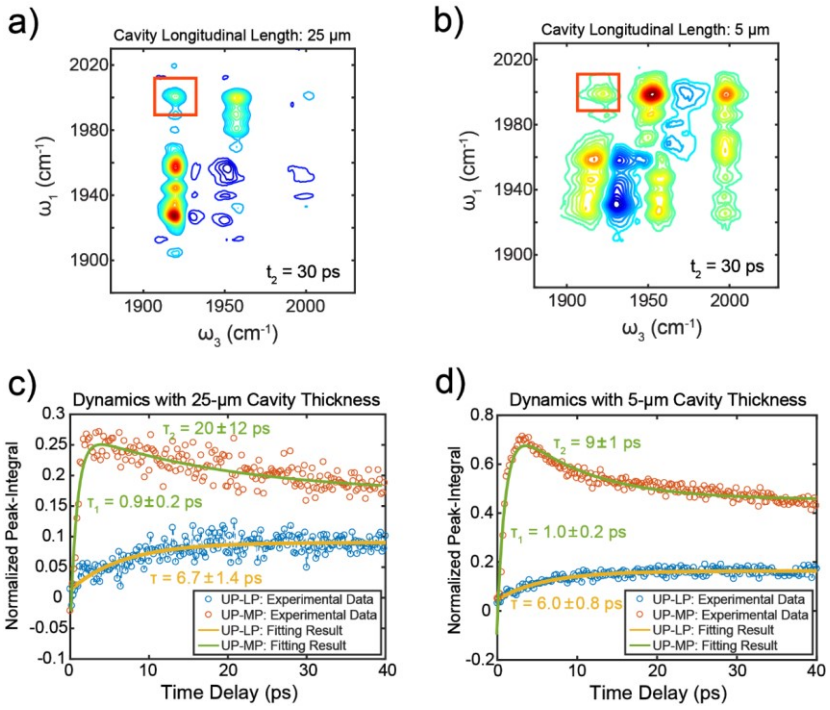

Fig. S6.

Cavity-thickness dependence. 2D IR spectra of strongly coupled saturated $W(CO)_6$+$W(^{13}CO)_6$ system at t_2 = 30 ps with cavity longitudinal length of (a) 25-μm and (b) 5-μm. UP narrow-pump transient pump-probe dynamics of strongly coupled saturated $W(CO)_6$+$W(^{13}CO)_6$ system at t_2 = 30 ps with cavity longitudinal length of (c) 25-μm and (d) 5-μm.

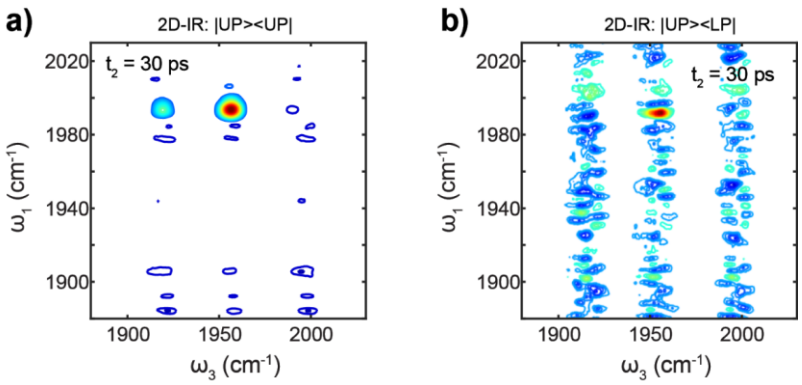

Fig. S7.

2D IR spectra with |UP><UP| and |UP><LP| narrow pump. 2D IR spectra of strongly-coupled saturated $W(CO)_6$+$W(^{13}CO)_6$ system with t_2 = 30 ps and 12-μm cavity thickness under the pumping condition of (a) both the first and second pump pulses are UP narrow-pumps and (b) the first pump pulse is UP-pump while the second pump pulse is LP-pump to create |UP><LP| coherence state.

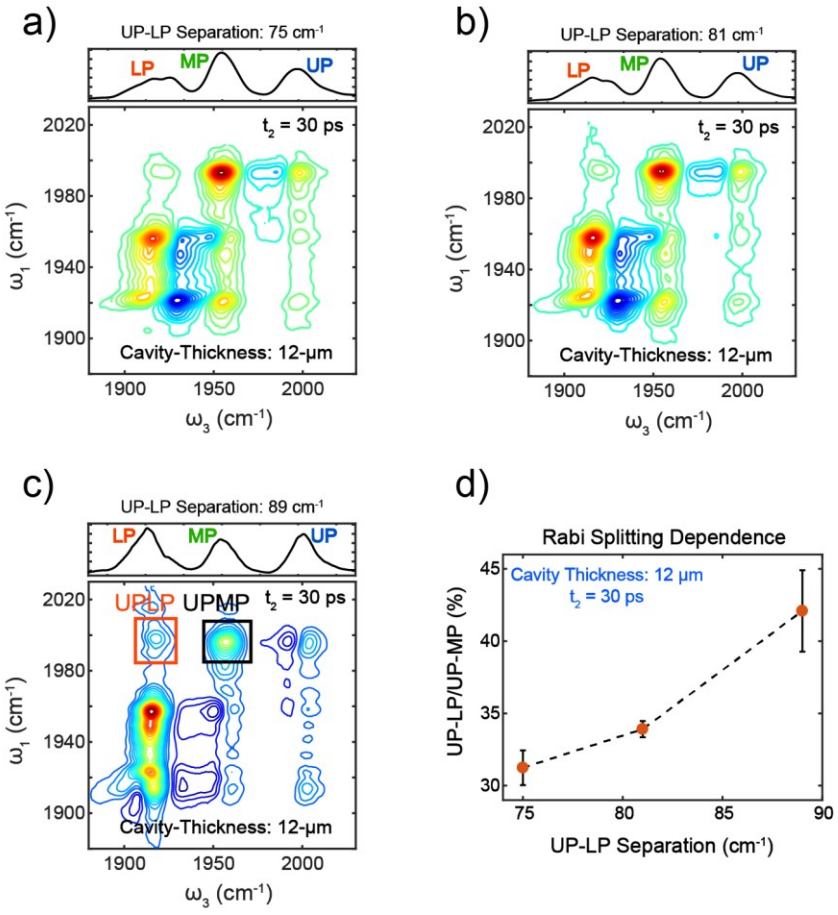

Fig. S8.

Molecular concentration dependence. 2D IR spectra of strongly coupled $W(CO)_6$+$W(^{13}CO)_6$ system at t_2 = 30 ps with cavity longitudinal length of 12-μm and Rabi splitting (UP-LP energy difference) of (a) 75 cm^{-1}, (b) 81 cm^{-1} and (c) 91 cm^{-1}. (d) Plot of UP-LP cross peak area (red box in a) relative to that of UP-MP (black box in a) as a function of UP-LP separation tuned by the molecular concentration at t_2 = 30 ps.

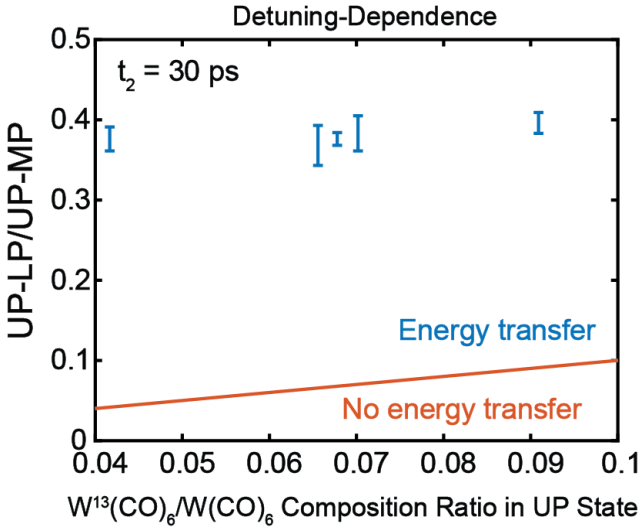

Fig. S9.
Cavity-detuning dependence. The ratio between UP-LP and UP-MP peak integrals plotted as a function of $W^{13}(CO)_6/W(CO)_6$ composition ratio in UP state at t_2 = 30 ps.

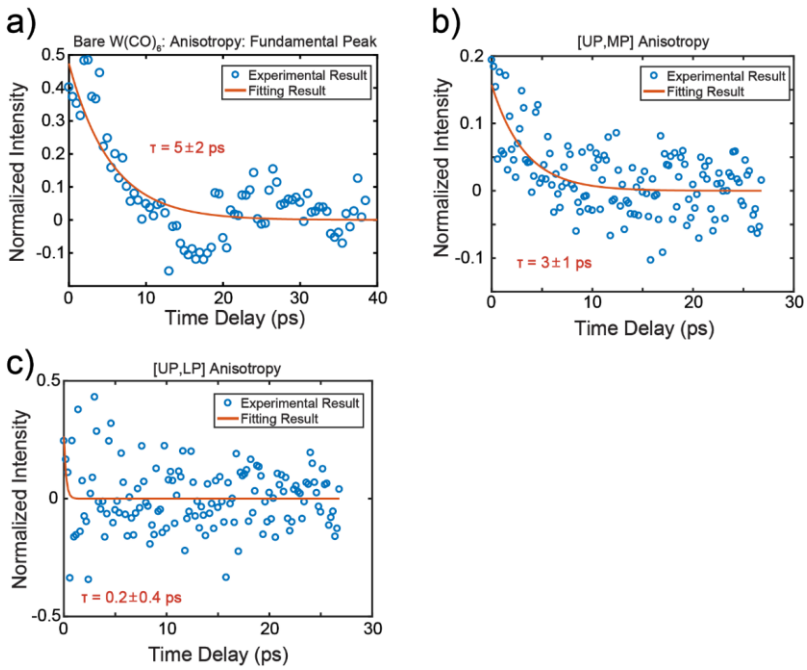

Fig. S10.

Anisotropy dynamics. Anisotropy decay trends of (a) Fundamental mode of bare $W(CO)_6$ molecules; (b) UP MP cross-peak and (c) UP-LP cross-peak where two molecular modes and one cavity mode are strongly coupled.

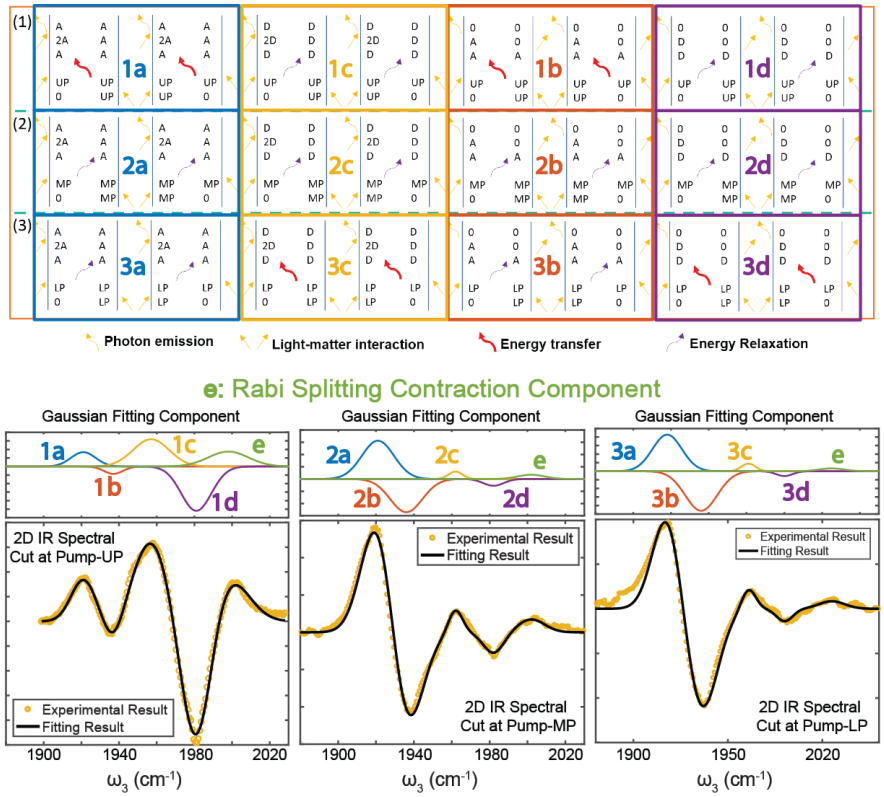

Figure S11.

Feynman diagrams. Top panel: Feynman diagrams of all quantum pathways in 2D IR spectra in Figure 2b. From (1) to (3) correspond to the systems are pumped to (1) UP/UP (2) MP/MP (3) LP/LP population states by the pump pulses. Then these population states evolve to acceptor/donor states within 30 ps. The vibrational energy transfer happens in first two quantum pathways in (1) UP/UP set while others experience an energy relaxation process. Bottom panel: Spectral cuts at pump-LP/MP/UP and their corresponding fitting results, showing the contributions from all the Feynman diagrams.

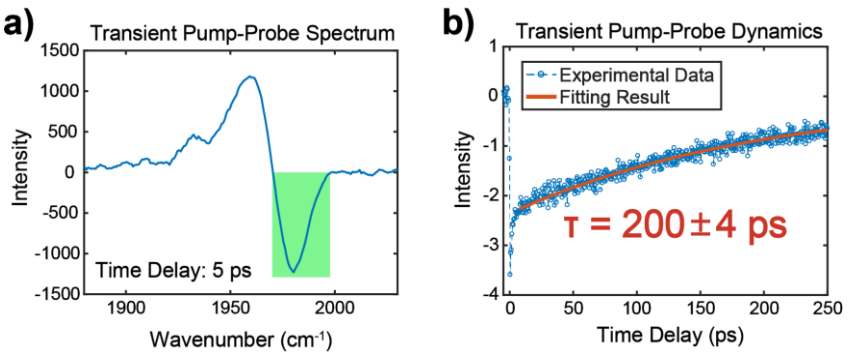

Fig. S12.

Vibrational dynamics of uncoupled system. (a) Transient pump-probe spectrum of uncoupled donor molecular system ($W(CO)_6$) where the green area represents its fundamental mode; (b) Pump-probe dynamics of the fundamental mode of donor

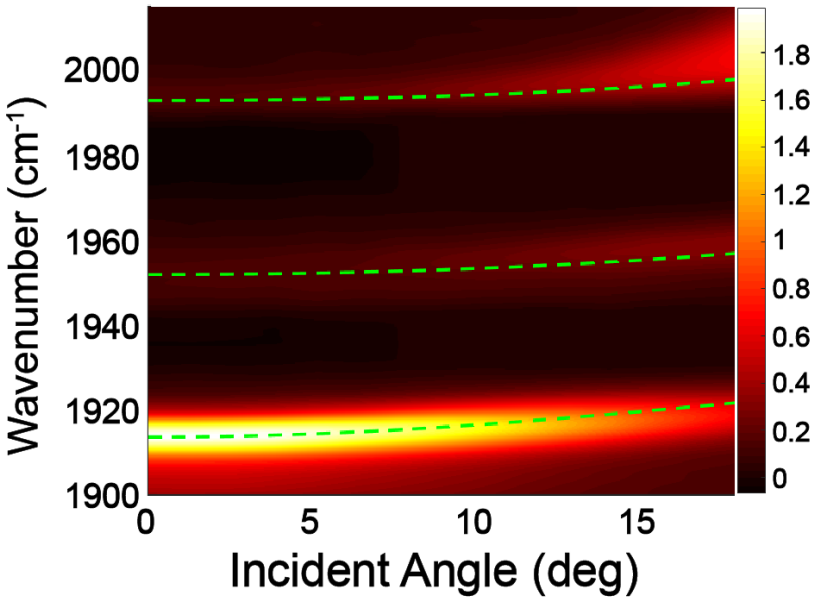

Fig. S13.
Dispersive curves of strongly coupled $W(CO)_6$+$W(^{13}CO)_6$ system with fitted UP, MP and LP angular dependent plots (dashed green lines).

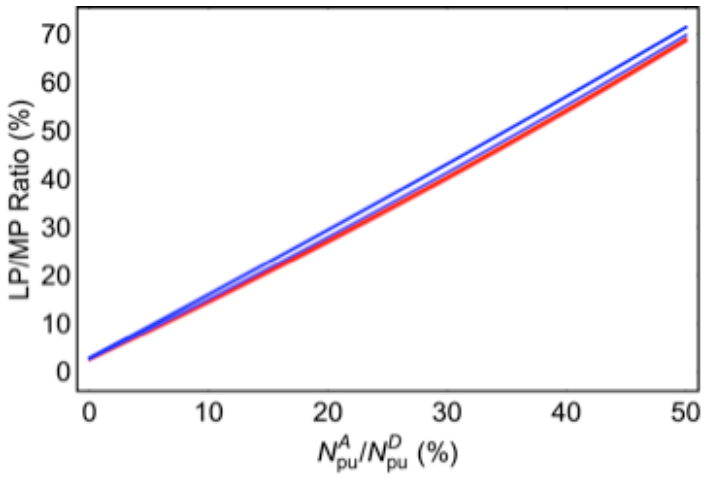

Fig. S14.

The ratio between areas under the LP and MP peaks for different ratios of excited acceptor [$W^{13}(CO)_6$.] to donor [$W(CO)_6$] populations computed with the generalization of Ref. (*11*) to a two-component molecular mixture strongly-coupled to a cavity field. The darker (lighter) blue curve corresponds to fixed $f^{D}_{pu} = 0.04$ (0.02), while the darker (lighter) red curve corresponds to fixed $f^{A}_{pu} = 0.01$ (0.005).

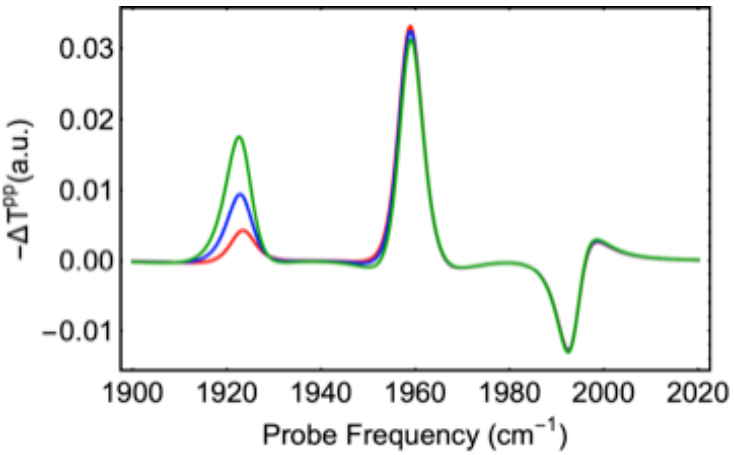

Fig. S15.
Differential pump-probe transmission computed with the generalization of Ref. (*11*) to a two-component molecular mixture strongly-coupled to a cavity field. All curves have $f_{pu}^{D} = 0.04$. The green, blue and red curves correspond to acceptor excited-state population fraction of 0.02, 0.01 and 0.004, respectively.

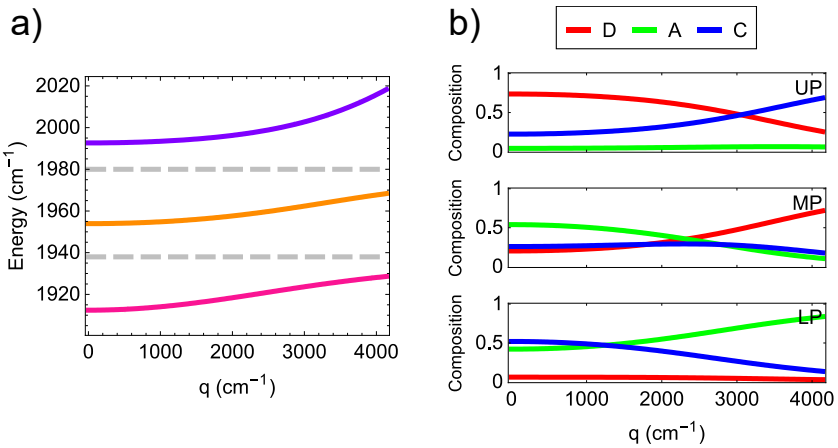

Fig. S16.
Simulated dispersion curves with Hopfield coefficients. (a) Calculated dispersion of strongly coupled system. Colored curves correspond to polariton states, and gray dashed curves correspond to dark states. (b) Hopfield coefficients of polariton states.

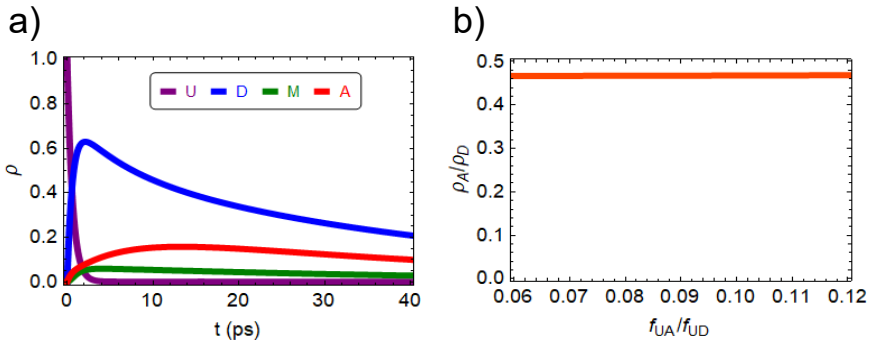

Fig. S17.
Simulated dynamics of strongly coupled system. (a) Population (ρ) dynamics when $UP_{q_{mid}}$ is pumped (i.e., $\rho_{U_{q_{mid}}}(0) = 1$, $\rho_{state \neq U_{q_{mid}}}(0) = 0$). q_{mid} is the in-plane wavevector at which the uncoupled cavity photon is equidistant in energy to E_D and E_A. (b) Ratio of A and D populations at t = 30 ps when UP_q is pumped (i.e., $\rho_{U_q}(0) = 1$, $\rho_{state \neq U_q}(0) = 0$) as a function of q, which is represented as the ratio f_{U_qA}/f_{U_qD} of Hopfield coefficients.

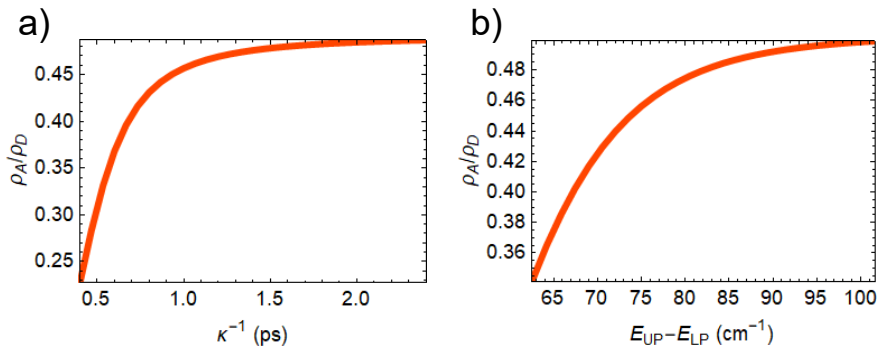

Fig. S18.
Peak ratio between A and D. Ratio of A and D populations as a function of (a) cavity lifetime and (b) concentration C of molecular species (expressed as the energy difference between UP and LP states with in-plane wavevector q_{mid}) when $UP_{q_{mid}}$ is pumped (i.e., $\rho_{U_{q_{mid}}}(0) = 1$, $\rho_{state \neq U_{q_{mid}}}(0) = 0$) q_{mid} is the in-plane wavevector at which the uncoupled cavity photon is equidistant in energy to E_D and E_A.

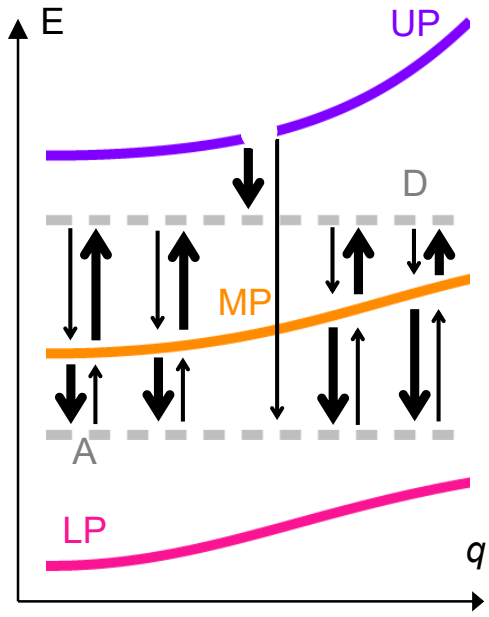

Fig. S19.
Schematic diagram illustrating VET mechanism suggested by kinetic model in Eqs. (S15)-(S18) and parameters in Table S2. Greater arrow thickness qualitatively represents a higher rate constant.

Vibrational Mode	Amplitude (a_i)	Peak-Position (b_i) in cm^{-1}	Width (c_i) in cm^{-1}
$W(CO)_6$ Mode	1.814	1982	9.151
$W(^{13}CO)_6$ Mode	1.788	1938	10.53

Table S1.
Lorentzian fit parameters for amplitudes, peak-positions, and widths.

Parameter	Assigned value
k_1	$(0.5\ ps)^{-1}$
k_2	$(3.55\ ps)^{-1}$
k_3	$(1.47\ ps)^{-1}$
γ_D	$(200\ ps)^{-1}$
γ_A	$(200\ ps)^{-1}$
κ	$(1.17\ ps)^{-1}$
E_D	$1980\ cm^{-1}$
E_A	$1938\ cm^{-1}$
Γ_D	$10\ cm^{-1}$
Γ_A	$10\ cm^{-1}$
L	9.2 μm
μ	0.75 D
n	1.4
C	50 mM

Table S2.
Parameters used in the kinetic model for the "reference setup".